The Astrophysical Journal, 889:50 (17pp), 2020 January 20 https://doi.org/10.3847/1538-4357/ab6333

Young Stars near Cometary Globule CG 30 in the Tumultuous Gum Nebula

Alexandra C. Yep and Russel J. White
Astronomy Department, Georgia State University, Atlanta, GA 30303, USA; ayep@astro.gsu.edu, white@chara.gsu.edu
Received 2018 October 9; revised 2019 December 9; accepted 2019 December 15; published 2020 January 24

Abstract

We have conducted a high-dispersion ($R \sim 34{,}000$) optical spectroscopic study of 10 young stars near the cometary globule CG 30 in the Gum Nebula, a diffuse H II region home to at least 32 cometary globules. All 10 spectroscopically observed stars at the nebula's northern edge are of low mass (spectral types M4.5–K5), have broad Hα emission, and show spectral veiling. Eight of the 10 are classical T Tauri stars. We spectroscopically measure the photospheric properties of CG 30 IRS 4 inside CG 30. Though embedded, CG 30 IRS 4 is T Tauri–like, with relatively slow projected rotation and moderate veiling. Undepleted Li absorptions, strong Hα emissions, and positions well above the main sequence on an H-R diagram suggest that the 10 stars are $\lesssim$1 Myr old. Using our measurements, previous spectroscopy, and previous photometry of 11 other young stars in the area, we determine stellar, kinematic, and accretion properties of a total of 21 young stars. Shared radial velocities, proper motions, distances, and ages suggest that 14 of the young stars (including CG 30 IRS 4) are kinematically related to CG 30. From *Gaia* DR2 distances to six of these stars, we derive a distance of 358.1 $\pm$ 2.2 pc to the cometary globule complex CG 30/31/38. The CG 30 association has an accretor fraction of 29% $\pm$ 14%, low for quiescent clusters of similar age but consistent with other irradiated clusters. The Gum Nebula's moderate radiation environment ($G_0 = 6.6^{+3.2}_{-2.7}$ at CG 30) may be strong enough to shorten disk lifetimes.

Unified Astronomy Thesaurus concepts: Young star clusters (1833); Cometary globules (276); Stellar accretion disks (1579); Protoplanetary disks (1300); Pre-main sequence (1289); Pre-main sequence stars (1290); Fundamental parameters of stars (555); Low mass stars (2050); Stellar accretion (1578); Stellar properties (1624); Accretion (14); Star forming regions (1565)

Supporting material: machine-readable tables

1. Introduction

The Gum Nebula is an extensive H II region centered near the extremely hot stars γ^2 Vel (WC8 + O7.5III), ζ Pup (O4fI), and, until recently, the progenitor of the supernova remnant Vela XYZ (Gum 1952; Brandt et al. 1971; Reipurth 1983; Pettersson 2007; Choudhury & Bhatt 2009). The massive stars irradiate surrounding cloud cores such that the cores' attenuated envelopes resemble comet tails, earning them the name *cometary globules* (Reipurth & Pettersson 1993). These photoevaporating objects may be precursors to Bok globules (Reipurth 1983; Bertoldi 1989; Sridharan 1992; Kim et al. 2005; Pettersson 2007; Maheswar & Bhatt 2008; Nakatani & Yoshida 2019). Cometary globules have been identified near OB associations (e.g., Orion Nebula, Rosette Nebula, Tr 37; Herbig 1974; Sicilia-Aguilar et al. 2013) but are particularly large, distinct, and numerous in the Gum Nebula, where at least 32 encircle the triangle formed by ζ Pup, γ^2 Vel, and Vela XYZ (Sridharan 1992; Kim et al. 2005; Choudhury & Bhatt 2009).

The ionizing radiation that shapes the cometary globules can be characterized by G_0, a region's far-UV (FUV) flux relative to the average interstellar medium (ISM) FUV flux $G_{0,\mathrm{ISM}} = 1.6 \times 10^3$ ergs s^{-1} cm^{-2} (Habing 1968; Winter et al. 2018). With ζ Pup at 335^{+12}_{-11} pc, γ^2 Vel at 349^{+44}_{-35} pc, and, until 11,000 yr ago, the progenitor of Vela XYZ at 294^{+76}_{-50} pc (Reipurth 1983; Caraveo et al. 2001; Apellániz et al. 2008), G_0 at cometary globule CG 30 at the Gum Nebula's northern edge is $6.6^{+3.2}_{-2.7}$ (see the Appendix for calculation). Such radiation from the three ionizing sources is vastly weaker than in the Orion Nebula Cluster (ONC) ($G_0 \sim 30{,}000$; Winter et al. 2018) or NGC 1977 in the Orion A cloud ($G_0 \sim 3{,}000$; Kim et al. 2016), but it is stronger than in quiescent Taurus ($G_0 \sim$ few) and may be powerful enough to enhance star formation rates and photoevaporate protoplanetary disks of the region's young stars (Bhatt 1993; Kim et al. 2005; Concha-Ramírez et al. 2019).

To investigate star formation in the area, Pettersson (1987) spectroscopically observed nine stars near CG 30 as part of an Hα prism survey (see Table 1). Four stars (including PHα 12 = KWW 1892, PHα 14 = KWW 975, and PHα 15 = 1043 in Kim et al. 2005) trace a dusty cloud near CG 30, and five trace a cloud near the background H II region RCW 19 (Rodgers et al. 1960; Pettersson 1987; see Figure 1). East of RCW 19 is another young star, IRAS 08159–3543, which appears abnormally luminous (Neckel & Staude 1995). All of these stars show an Hα emission width in excess of 10 Å (Pettersson 1987; Kim et al. 2005). Kim et al. (2005) studied 10 additional stars near CG 30 as part of an X-ray survey, and nine of them show Hα emission, strong Li absorption, or both. Kim et al. (2005) suggested that 11 young stars (including three from Pettersson 1987) are related to each other and CG 30, which itself contains five known infrared sources, two of which (IRS 3 and IRS 4) are near the Herbig–Haro object HH 120 (Pettersson 2007). A wide protobinary system powers the Herbig–Haro object (Reipurth 1983; Chen et al. 2008).

To understand this population more completely, we perform high-dispersion optical spectroscopy on the nine young stars from Pettersson (1987) and CG 30 IRS 4 to measure their rotational and radial velocities, Li absorption, and accretion properties. We also gather photometry from the Two Micron All Sky Survey (2MASS; Skrutskie et al. 2006) and data from *Gaia* DR2 (Gaia Collaboration et al. 2016, 2018) for these 10 stars, the 10 additional stars from Kim et al. (2005), and the one

Table 1
Basic Properties

Star Name	R.A. 2000[b] (h:m:s)	Decl. 2000[b] (deg:arcmin:arcsec)	Spectral Type[a]	V[a] (mag)	K[a] (mag)
PHα 12	08 08 22.15	−36 03 47.07	M1.5	15.206 ± 0.029	10.323 ± 0.021
PHα 14	08 08 33.87	−36 08 10.00	M2	15.85 ± 0.22	10.299 ± 0.023
PHα 15	08 08 46.82	−36 07 52.69	M3	15.61 ± 0.84	10.628 ± 0.024
PHα 21	08 10 30.91	−36 01 46.39	M4	16.42 ± 0.13	11.058 ± 0.023
PHα 34	08 12 47.05	−36 19 17.90	K3	15.16 ± 0.29	11.031 ± 0.023
PHα 40	08 13 51.69	−36 14 01.32	M0.5	16.547 ± 0.080	11.326 ± 0.021
PHα 41	08 13 56.08	−36 08 01.96	Cont.	14.3 ± 1.1	8.914 ± 0.024
PHα 44	08 14 21.96	−36 10 03.38	K7–M0	16.004 ± 0.045	11.713 ± 0.019
PHα 51	08 15 55.31	−35 57 58.19	K7–M0	16.17 ± 0.37	11.090 ± 0.023
CG 30 IRS 4	08 09 33.16	−36 04 57.81	⋯	⋯	12.077 ± 0.044

Notes.
[a] Pettersson (1987).
[b] 2MASS.
(This table is available in machine-readable form.)

luminous star from (Neckel & Staude 1995). In all, we examine the stellar properties, accretion properties, kinematics, and possible associations of 21 young stars near CG 30 and RCW 19.

In Section 2 we discuss observations taken with the Keck I telescope's high-resolution spectrometer. In Section 3 we plot our spectra and present Li and Hα equivalent widths, radial velocities, rotational velocities, spectral types, and veiling, which is a filling-in of spectral lines caused by accretion (Hartigan et al. 1989). We correct the photometry for veiling and reddening in Section 4 to calculate extinctions and luminosities and plot an H-R diagram. We discuss kinematic association and accretor fractions in Section 5 and summarize in Section 6. The Appendix shows how we quantify the FUV radiation at CG 30.

2. Observations

2.1. Keck HIRES Spectra

We observed the 10 young stars using the High-Resolution Echelle Spectrometer (HIRES; Vogt et al. 1994) on the W. M. Keck I telescope on 2003 February 17, 2003 February 18, and 2004 April 4. We obtained one epoch for PHα 12, 14, 15, 21, 40, 44, and 51, two epochs for PHα 34, and three epochs for PHα 41 and CG 30 IRS 4. All observations were obtained prior to the HIRES CCD upgrade in 2004, so light was recorded on the former Tektronix 2048 CCD. We used the red collimator and the RG-610 filter. Light was projected through the D1 decker (1″ 15.″14″ 00), slit width 4 pixels, yielding a resolving power of ∼34,000. The cross-disperser and echelle angles were set at approximately 1°41 and −0°28, respectively, to achieve a wavelength coverage of 6300–8750 Å, spanning 16 orders with 20–80 Å gaps between the orders. Each night, we obtained an internal quartz lamp for flat-fielding and a ThAr lamp for wavelength calibration.

We note that our setup is identical to that used in the spectroscopic study of young stars in Taurus–Auriga (White & Hillenbrand 2004). From this previous study, we have a wide range of K- and M-type standards and several young stars observed in an identical fashion for reliable comparisons.

2.2. Reduction and Extraction

The HIRES data were reduced using the facility *makee* reduction script written by T. Barlow. The reductions included bias subtraction, flat-fielding, spectral extraction, sky subtraction, and wavelength calibration. The spectra were interpolated onto a log-linear scale for cross-correlation purposes. With the exception of CG 30 IRS 4, the projected spectra have spatial profiles with FWHMs of ∼2″, set by the seeing at the elevation of these low-latitude targets (decl. −36°20′ to −35°57′). Here CG 30 IRS 4 is slightly spatially extended; some of the visible light is likely scattered off the nebula. For all stars, we calibrate the wavelength solution using the telluric A band at 7600–7630 Å, which should remain stable down to 0.015 km s^{-1} (Cochran 1988).

3. Spectroscopic Analysis

Five spectral regions of interest are displayed in Figures 2 and 3, including temperature-sensitive Ca, Fe, and TiO and gravity-sensitive K I. All 10 stars show Li I λ6708 absorption (Figure 2, second column) and Hα emission (Figure 4). The stars PHα 34 and 41 show particularly strong Hα emission and a myriad of other emission lines, including Ca I λ6455, Fe II λ6456, K I λ7700, and O I λ8446. Observations of PHα 41 on two consecutive nights reveal that it is a double-lined spectroscopic binary with a period $\lesssim$2 days; the components swap redward and blueward positions and are well separated in velocity.

3.1. Li I λ6708 Equivalent Width

Because of deep convection, significant depletion of atmospheric lithium takes 10–20 Myr for mid-M-type stars and ∼100 Myr for early K-type stars (Jeffries et al. 2014). As a first assessment of youth, we measure Li I λ6708 equivalent widths W_λ(Li) using IRAF's Gaussian-fitting *splot* package. Uncertainties stem from ambiguity in the local continuum, with a minimum uncertainty of 0.01 Å imposed to account for systematics.

We report Li equivalent widths from all epochs and include the two data in Kim et al. (2005) for reference (see Table 2). The majority of the stars show lithium equivalent widths 0.5–0.6 Å, similar to stars with no lithium depletion in Taurus–Auriga (e.g., Basri et al. 1991; Magazzú et al. 1992; Martín et al. 1994) or

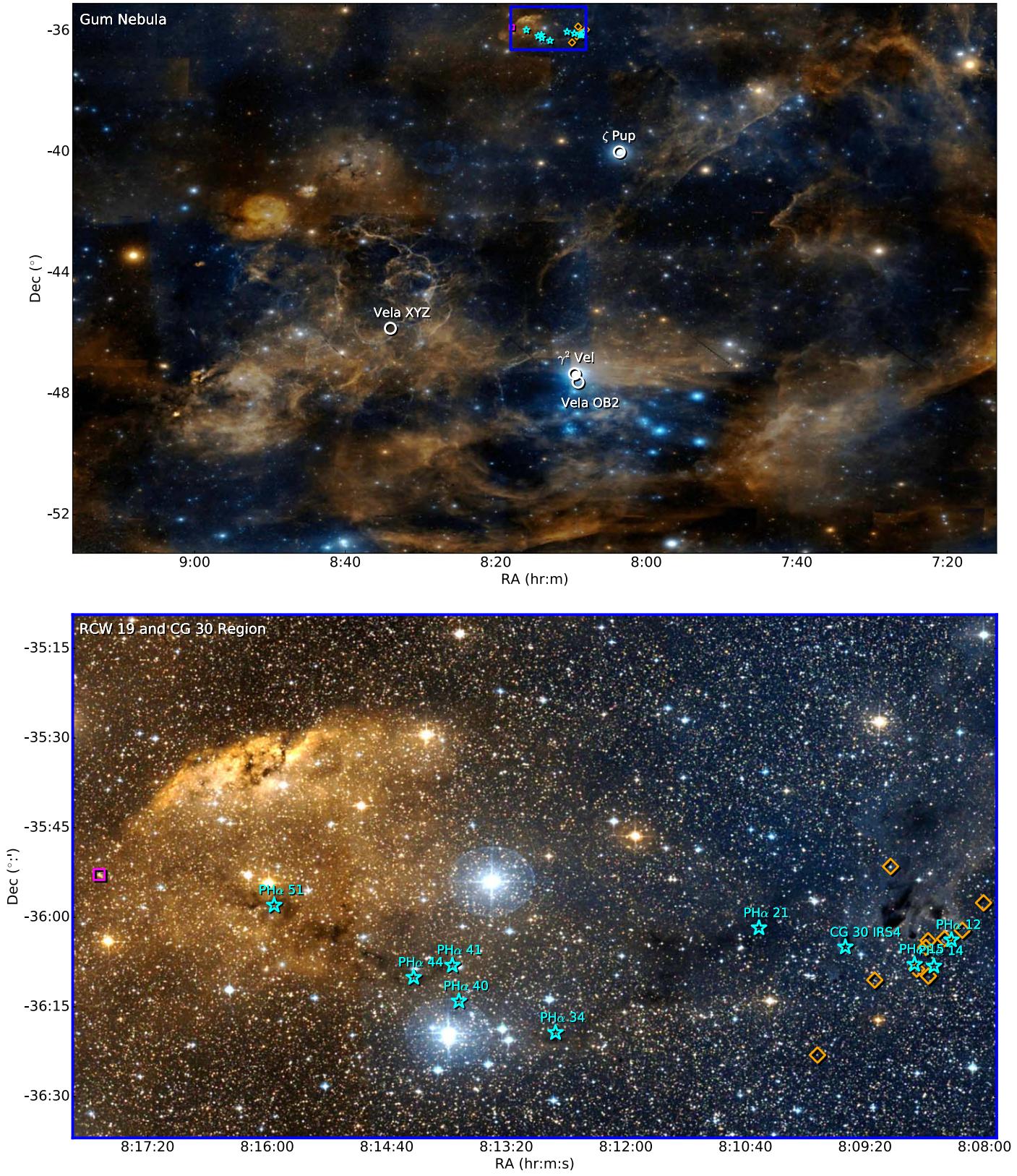

Figure 1. The top panel displays the main potential ionizers of the Gum Nebula (white circles), namely the O-type stars ζ Pup and γ^2 Vel, OB association Vela OB2, and supernova remnant Vela XYZ. The target young stars (cyan star symbols from Pettersson 1987, orange diamonds from Kim et al. 2005, and magenta square from Neckel & Staude 1995) lie at the Gum Nebula's northern edge (blue box). This region is enlarged in the bottom panel. Four PHα young stars, CG 30 IRS 4, and 10 KWW stars trace dust near the cometary globule CG 30 of the CG 30/31/38 cometary globule complex. Five PHα stars and one star from Neckel & Staude (1995) trace dust spatially near the H II region RCW 19. The background images have been generated in Aladin using DSS2 (red, blue, infrared), and star locations have been plotted in PyPlot.

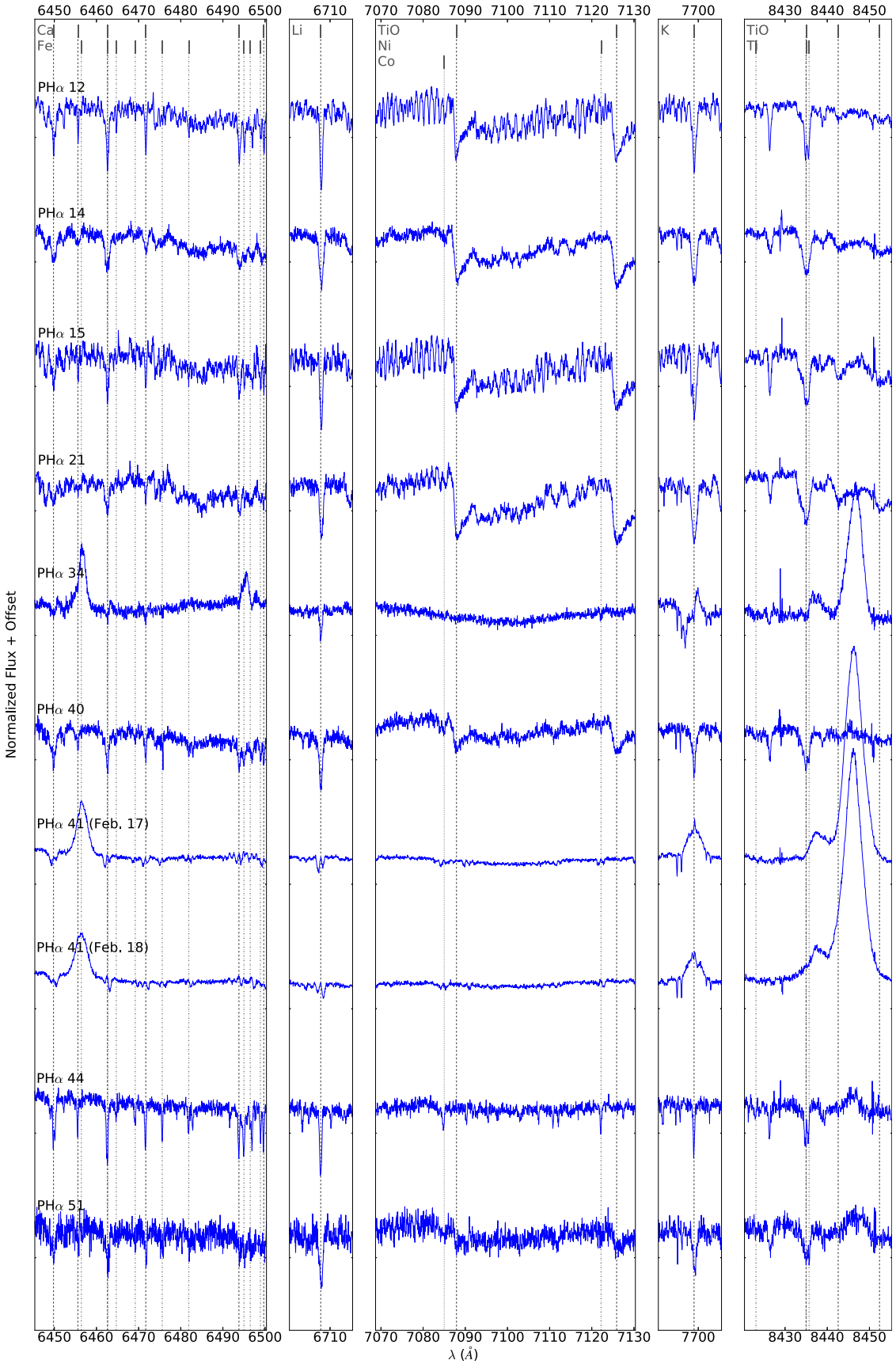

Figure 2. Five spectral regions of interest are displayed for the nine PHα stars. Spectral features are labeled at the top of the figure. The first and fifth columns show Ca, Fe, and Ti, typically strong in K-type stars (e.g., PHα 44). The third column shows TiO molecular bands, wide and deep for M-type stars (e.g., PHα 14). The second column shows lithium absorption, associated with young stars. The fourth column tracks surface gravity with K I λ7700, which is relatively weak for young stars still in the process of gravitationally settling. All of the stars in our sample exhibit a shallowing of spectral lines and bands called veiling.

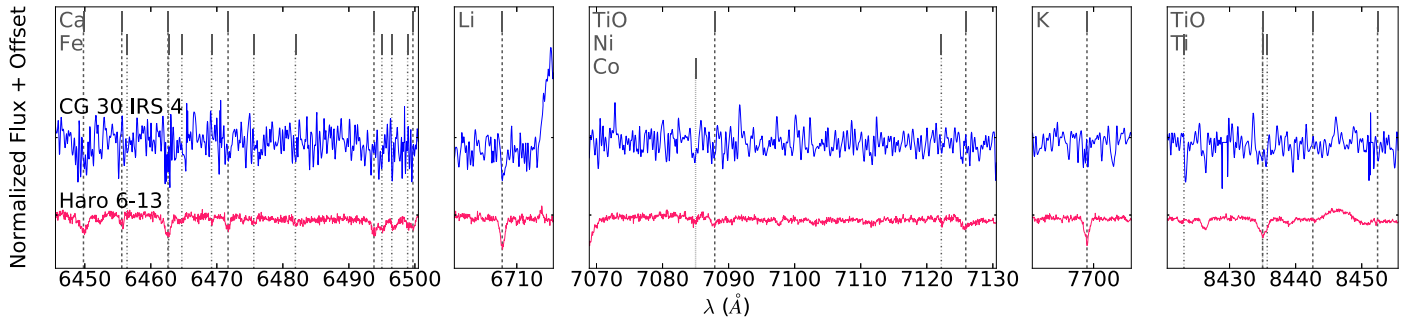

Figure 3. We compare the same five spectral regions of interest as in Figure 2 for the embedded star CG 30 IRS 4 (blue, smoothed) and veiled T Tauri star Haro 6–13 (fuchsia) of the same spectral type, M0 (White & Hillenbrand 2004). The infrared source inside the cometary globule has a well-defined photosphere.

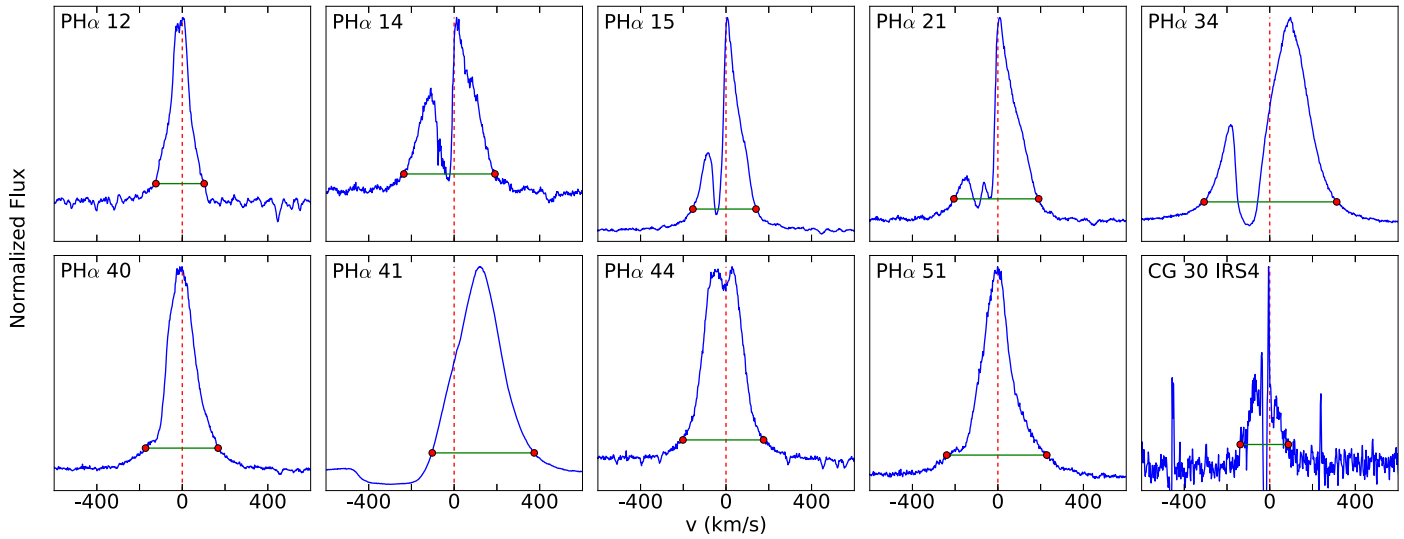

Figure 4. We measure Hα widths at 10% up the peak (green lines). Red dashed lines mark zero-velocity 6562.8 Å. Blueshifted dips within the emission peaks are likely absorption lines from cool winds.

Orion (e.g., Palla et al. 2005, 2007) at ages of 1–3 Myr. The two stars with much smaller equivalent widths are substantially veiled (PHα 34) or veiled and have a spectroscopic companion (PHα 41). The highest lithium equivalent width is shown by CG 30 IRS 4. However, the continuum level of CG 30 IRS 4 is more difficult to determine than that of other stars.

3.2. Hα 10% Widths and Equivalent Widths

White & Basri (2003) demonstrated that the width of the Hα emission profile at 10% peak height above the continuum, W_{10}(Hα), more reliably distinguishes classical T Tauri stars (accreting) from weak-line T Tauri stars (nonaccreting) than Hα equivalent width, W_λ(Hα). Using Python, we measure $W_{10}(\mathrm{H}\alpha) = 225$–$621\ \mathrm{km\ s^{-1}}$ (see Table 2). Based on the accretion criterion $W_{10}(\mathrm{H}\alpha) > 270\ \mathrm{km\ s^{-1}}$ (White & Basri 2003), eight of our targets are classical T Tauri stars, while PHα 12 is a weak-line T Tauri star ($W_{10}(\mathrm{H}\alpha) = 226\ \mathrm{km\ s^{-1}}$), although only slightly below the classical T Tauri limit. Surprisingly, embedded CG 30 IRS 4 ($W_{10}(\mathrm{H}\alpha) = 225\ \mathrm{km\ s^{-1}}$) also falls below the classical T Tauri star limit. However, as noted previously, the continuum level of CG 30 IRS 4 is ambiguous. This binary star also has jets and outflow (Chen et al. 2008) that might absorb some of its Hα emission. Because PHα 41 exhibits blueshifted absorption that drops below the continuum, its 10% widths are lower limits for the whole binary.

We also measure W_λ(Hα) using IRAF as described for Li I λ6708 (Section 3.1). The revealed young stars' W_λ(Hα) values range from −83 to −11.5 Å, similar to those of accreting T Tauri stars. Embedded CG 30 IRS 4 has the weakest emission, −6.6 to −0.5 Å. Our values for W_λ(Hα) differ from previous values by up to a factor of two. This is fairly typical of young stellar objects, which tend to vary over short timescales (Pettersson 1987; Kim et al. 2005).

3.3. Radial Velocity

Radial velocities are obtained relative to a catalog of G-, K-, and M-type dwarf standards (see Section 2.1) with radial velocities accurate to 0.3–0.4 $\mathrm{km\ s^{-1}}$ (Nidever et al. 2002; Valenti & Fischer 2005), slow rotation $\leqslant 3\ \mathrm{km\ s^{-1}}$ (Delfosse et al. 1998; Valenti & Fischer 2005), no disks, and no veiling. Through cross-correlation analysis of the Doppler shifts for between seven and eleven spectral regions (see Figure 2), we measure velocities relative to between five and seven standards of similar spectral type to each young star. We also measure the Doppler shift of the Li I λ6708 absorption feature using the T Tauri stars DN Tau and V 836 Tau with known radial velocities (White & Hillenbrand 2004). Star spots on DN Tau and V 836 Tau may introduce velocity oscillations of $1\ \mathrm{km\ s^{-1}}$ or less (Prato et al. 2008). For some of our young stars, including CG 30 IRS 4, Li I λ6708 is the most prominent absorption feature.

Table 2
Equivalent Widths

Star Name	Date Obs.	Lit.[a,b] W_λ(Hα) (Å)	Our W_λ(Hα) (Å)	W_{10}(Hα) (Å)	W_{10}(Hα) (km s^{-1})	Lit.[b] W_λ(Li I) (Å)	Our W_λ(Li I) (Å)
PHα 12	2004 Apr 4	−16.1, −26.6	−11.5 ± 0.6	−4.94	226	0.54 ± 0.04	0.57 ± 0.01
PHα 14	2004 Apr 4	−22.0, −8.43	−12.9 ± 0.3	−9.33	427	0.50 ± 0.06	0.57 ± 0.02
PHα 15	2004 Apr 4	−130.5	−45.4 ± 2.9	−6.46	295	⋯	0.51 ± 0.01
PHα 21	2004 Apr 4	−48.1	−28.9 ± 1.0	−8.68	397	⋯	0.51 ± 0.01
PHα 34	2003 Apr 17	−60.5	−61.8 ± 3.2	−13.58	621	⋯	0.21 ± 0.01
	2004 Apr 4		−71.8 ± 3.8	−12.65	579		0.30 ± 0.01
PHα 40	2004 Apr 4	−18.7	−33.0 ± 0.8	−7.43	340.	⋯	0.53 ± 0.02
PHα 41 A	2003 Feb 17	−98.6	−78.5 ± 9.3[c]	<−10.44[c]	>478[c]	⋯	0.05 ± 0.01
	2003 Feb 18		−83 ± 10.[c]	<−10.07[c]	>461[c]		0.07 ± 0.01
	2004 Apr 4		−80.4 ± 5.7[c]	<−11.73[c]	>537[c]		0.05 ± 0.01
PHα 41 B	2003 Feb 17	−98.6	−78.5 ± 9.3[c]	<−10.44[c]	>478[c]	⋯	0.10 ± 0.01
	2003 Feb 18		−83 ± 10.[c]	<−10.07[c]	>461[c]		0.11 ± 0.01
	2004 Apr 4		−80.4 ± 5.7[c]	<−11.73[c]	>537[c]		0.08 ± 0.01
PHα 44	2004 Apr 4	−50.7	−27.8 ± 0.9	−8.26	378	⋯	0.43 ± 0.01
PHα 51	2003 Feb 18	−70.1	−54.7 ± 2.1	−10.25	469	⋯	0.62 ± 0.06
CG 30 IRS 4	2003 Feb 17	⋯	−0.5 ± 1.4	−5.26	241	⋯	0.47 ± 0.82
	2003 Feb 17		−3.5 ± 1.2	−4.98	228		0.60 ± 0.38
	2003 Feb 18		−6.6 ± 1.8	−4.93	225		0.67 ± 0.11

Notes.
[a] Pettersson (1987).
[b] Kim et al. (2005).
[c] Because the two Hα emission components cannot be resolved, we give Hα emission values for the whole binary (see text).
(This table is available in machine-readable form.)

Table 3
Radial and Rotational Velocities

Star Name	v_r (km s^{-1})	$v_{\rm rot}\sin(i)$ (km s^{-1})
PHα 12	23.07 ± 0.15	8.0 ± 0.6
PHα 14	26.77 ± 0.89	27.8 ± 2.7
PHα 15	21.99 ± 0.20	11.2 ± 0.5
PHα 21	24.12 ± 0.21	20.4 ± 1.1
PHα 34	31.65 ± 0.29	12.7 ± 0.5
PHα 40	32.16 ± 0.29	13.2 ± 0.8
PHα 41 A	29.69 ± 0.41[a]	14.4 ± 0.7
PHα 41 B	29.69 ± 0.41[a]	10.7 ± 1.2
PHα 44	30.29 ± 0.15	8.3 ± 0.6
PHα 51	33.69 ± 0.44	10.6 ± 1.1
CG 30 IRS 4	22.5 ± 2.0	6.3 ± 0.2

Note.
[a] The reported v_r for PHα 41 A and B is the systemic velocity of the pair (see text).
(This table is available in machine-readable form.)

Table 4
PHα 41 A and B Velocities across Three Epochs

MJD	v_r (km s^{-1}) A	v_r (km s^{-1}) B	$v_{\rm rot}\sin(i)$ (km s^{-1}) A	$v_{\rm rot}\sin(i)$ (km s^{-1}) B
52,687.47	4.27 ± 0.19	51.7 ± 1.3	16.4 ± 1.1	12.6 ± 3.1
52,688.48	58.49 ± 0.44	1.1 ± 1.5	14.4 ± 1.4	9.0 ± 1.4
53,099.35	63.73 ± 0.32	−0.7 ± 1.5	11.8 ± 1.2	17.2 ± 3.0

(This table is available in machine-readable form.)

Using the uncertainty-weighted mean of the median relative velocities from all spectral regions, we calculate radial velocities v_r relative to the center of mass of the solar system. Stars within 20′ of CG 30 have $v_r = 21.99$–$26.77\,{\rm km\,s^{-1}}$, whereas stars within 30′ of PHα 41 have $v_r = 30.29$–$33.69\,{\rm km\,s^{-1}}$ (see Table 3). We obtain uncertainties of 0.15–0.89 km s^{-1}.

Special handling is required for PHα 41 and CG 30 IRS 4. For PHα 41, since the components are well separated in velocity, we isolate and independently measure one member of the binary at a time. An overabundance of emission lines forces us to use just two to four spectral regions to measure the relative velocities of each star. The v_r uncertainties across all three epochs are 0.19–0.44 km s^{-1} for A and 1.3–1.5 km s^{-1} for B (see Table 4).

To calculate the binary's systemic v_r, we take the two stars' masses from Pecaut & Mamajek (2013) based on their spectral types, $0.72\,M_\odot$ for the K5 primary and $0.70\,M_\odot$ for the K6 secondary. The center-of-mass velocity is then

$$v_{r,\rm cm} = \frac{m_A}{m_A + m_B} v_{r,A} + \frac{m_B}{m_A + m_B} v_{r,B}. \quad (1)$$

The v_r errors of the two stars are added in quadrature. We take the error-weighted mean of the three nights' results for a final systemic $v_r = 29.69 \pm 0.41\,{\rm km\,s^{-1}}$.

To combat CG 30 IRS 4's low signal-to-noise ratio (4–12), we have smoothed the spectra across each 1 Å using IRAF's *dispcor* routine before performing cross-correlation. Stellar features are visible in all three epochs, including strong lithium absorption and several Ca and Fe lines (Figure 3). We obtain $v_r = 22.5 \pm 2.0\,{\rm km\,s^{-1}}$.

3.4. Rotational Velocity

We derive the stars' projected rotational velocities $v_{\rm rot}\sin(i)$ from the widths of the cross-correlation functions described in the previous section. We artificially broaden the standard spectra following Gray (1992), assuming a limb-darkening coefficient $\epsilon = 0.6$, until the width of the standard's auto-correlation peak matches the width of the standard's cross-correlation peak with the young star. As with v_r, we take the error-weighted mean of the five to seven standards' rotational velocity medians of the seven to eleven spectral regions. We estimate the uncertainty from the standard deviation of the median values. Because the velocity resolution and rotation uncertainties add in quadrature, we assume a minimum measurement limit of $\sim 8.8/\sqrt{2} = 6.2\,{\rm km\,s^{-1}}$. Measured values $<6.2\,{\rm km\,s^{-1}}$ are set to $6.2\,{\rm km\,s^{-1}}$. All median values are larger than this number, so specifying this resolution limit does not affect the final $v_{\rm rot}\sin(i)$; it serves chiefly to constrain the final uncertainties.

We obtain $v_{\rm rot}\sin(i) = 6.3$–$27.8\,{\rm km\,s^{-1}}$ (see Table 3). That of CG 30 IRS 4 is the lowest. The uncertainties are 0.2–2.7 $\rm km\,s^{-1}$. We measure the $v_{\rm rot}\sin(i)$ of PHα 41's two components separately, as detailed above for v_r.

3.5. Veiling and Spectral Types

The accretion of circumstellar gas produces extra light at UV and optical wavelengths and diminishes the depths of spectral lines, or veils them (Hartigan et al. 1989; Hartmann et al. 2016; Rei et al. 2018). We measure this veiling as the ratio of continuum excess to photospheric continuum, $r = F_{\rm ex}/F_{\rm phot}$ (Hartigan et al. 1989). Veiling is wavelength-dependent and tends to be stronger at bluer wavelengths (Hartigan et al. 1991). We measure the average veiling r_{6500} in four spectral regions near 6500 Å to trace the continuum excess in the R band and r_{8400} in three regions near 8400 Å for the I band.

Measuring veiling involves adding a flat, featureless continuum to a standard star's spectrum and renormalizing the spectrum until its lines are shallow enough to match the young star spectrum. Doing so requires properly accounting for v_r and $v_{\rm rot}\sin(i)$. Figure 5 illustrates the process for the M3.5V-type standard GL 669 A and young star PHα 14.

Measurement of veiling is sensitive to absorption strength and thus assigned spectral type. While the minimum rms results of the cross-correlation procedure recommend likely spectral types, all spectral types are confirmed through visual inspection of line strengths, line ratios, and TiO band depths. We find spectral types M4.5 to K5, with uncertainties of 0.5 spectral class for M-type stars and one spectral class for K-type stars (see Table 5). The spectral types we assign differ somewhat from those given in Pettersson (1987) but are based on higher-resolution spectra and account for veiling.

Veiling uncertainties are derived from the sample standard deviation to veiling values from spectral types 0.5–1 classes above and below the assigned spectral type. We impose a veiling uncertainty lower limit of 0.10 to account for systematics.

Once again, PHα 41 A and B (spectral types K5 and K6) are handled specially. Light from the companion contaminates each star's measured continuum excess, causing the above procedure to overestimate the veiling. What we measure for PHα 41 A and B are $r_A = (F_{\rm ex}{+}F_B)/F_A$ and $r_B = (F_{\rm ex}{+}F_A)/F_B$, where $F_{\rm ex}$ is the combined continuum excesses of both stars: $F_{\rm ex} = F_{{\rm ex},A}{+}F_{{\rm ex},B}$; there is no way to determine the relative contribution of each to the total excess with this analysis. We define the combined veiling for each star as follows:

$$r'_A = \frac{F_{ex}}{F_A} = r_A - \frac{F_B}{F_A}, \tag{2}$$

$$r'_B = \frac{F_{ex}}{F_B} = r_B - \frac{F_A}{F_B}, \tag{3}$$

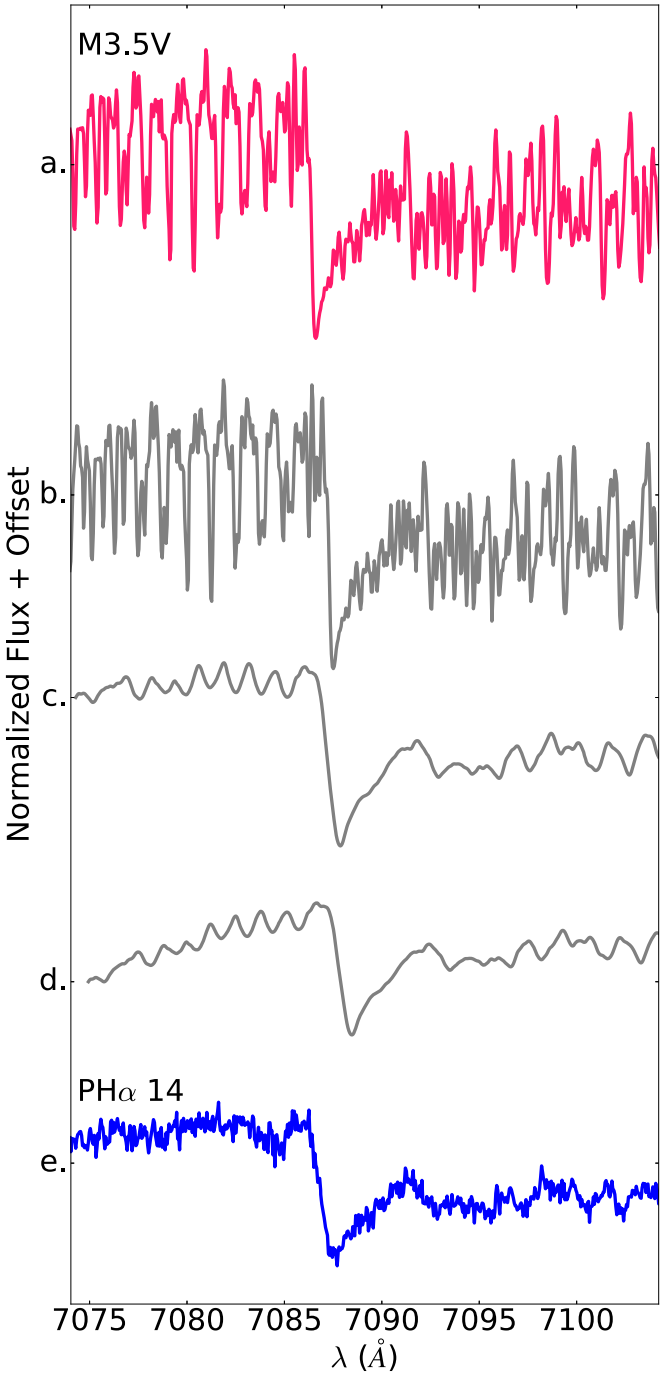

Figure 5. The M3.5V standard spectrum ((a), fuchsia) is manipulated (gray) with v_r shift (b), rotational broadening (c), and veiling (d) until it matches the young star spectrum of PHα 14 ((e), blue).

Table 5
Veiling and Spectral Types

Star Name	Spectral Type	r_{6500}	r_{8400}
PHα 12	M3 ± 0.5	0.16 ± 0.13	0.020 ± 0.10
PHα 14	M3.5 ± 0.5	0.21 ± 0.18	0.00 ± 0.10
PHα 15	M4 ± 0.5	0.20 ± 0.15	0.00 ± 0.20
PHα 21	M4.5 ± 0.5	0.29 ± 0.10	0.31 ± 0.37
PHα 34	K7 ± 1.0	6.04 ± 0.63	3.1 ± 1.7
PHα 40	M0.5 ± 0.5	0.67 ± 0.11	0.45 ± 0.10
PHα 41 A	K5 ± 1.0	5.24 ± 0.22	3.62 ± 0.33
PHα 41 B	K6 ± 1.0	7.49 ± 0.10	7.54 ± 0.10
PHα 44	K5 ± 1.0	0.21 ± 0.10	0.15 ± 0.14
PHα 51	M0.5 ± 0.5	0.94 ± 0.15	1.36 ± 0.51
CG 30 IRS 4	M0 ± 1.0	0.86 ± 0.10	0.15 ± 0.20

(This table is available in machine-readable form.)

where we know the flux ratios of the two photospheres from their spectral types K5 and K6: $F_A/F_B = 1.629$ (Pecaut & Mamajek 2013). It is these combined veiling values r_A' and r_B' that we report for PHα 41 A and B, respectively.

Veiling values range from 0.16 to 0.94 near 6500 Å and 0.0 to 1.36 near 8400 Å for most of the 10 young stars (see Table 5). The values soar to 3.1–7.54 for PHα 34, 41 A, and 41 B, the stars with abundant emission lines. The presence of numerous emission lines is associated with strong accretion and possibly a second source of veiling. In addition to continuum veiling from accretion-fed hot spots on the star, line-dependent veiling can result from abnormal chromospheric structures heated by particularly powerful accretion (Rei et al. 2018). Moderate veiling is shown in CG 30 IRS 4 (spectral type M0), 0.86 ± 0.10 near 6500 Å and 0.15 ± 0.20 near 8400 Å.

4. Stellar Properties

The determined spectroscopic properties of the nine PHα stars and CG 30 IRS 4 are used in combination with photometry and parallax measurements to estimate their stellar luminosities and temperatures for comparison with stellar evolutionary models. We add 10 pre-main-sequence G-, K-, and M-type stars identified by Kim et al. (2005) to our analysis, for which Kim et al. (2005) provided spectroscopic and photometric results. The stars KWW 975, 1043, and 1892 are already included in our analysis as PHα 14, 15, and 12. Eleven of the 13 young stars studied by Kim et al. (2005) are believed to be dynamically related to CG 30. We also look at the star IRAS 08159–3543 near RCW 19 (see Figure 1), known to power a bipolar wind and ascribed an incredible luminosity of 24,000 $L_\odot$ (Neckel & Staude 1995; Bronfman et al. 1996). In all, we photometrically examine 21 young stars.

4.1. Photometry

We flux-average Johnson–Cousins *UBVRI* photometry from Pettersson (1987) and Kim et al. (2005; see Table 1 for *V* magnitudes). We propagate the fluxes' sample standard deviations into magnitude uncertainties. Because PHα 15 and PHα 41 vary by more than 1.5 mag, their magnitude uncertainties are large, 0.84 and 1.1 mag, respectively.

For all 21 stars from Pettersson (1987), Neckel & Staude (1995), and Kim et al. (2005), we gather *J*, *H*, and *K* magnitudes from 2MASS. The stars CG 30 IRS 4, KWW XRS 9, and IRAS 08159–3543 have only infrared photometry. For CG 30 IRS 4, 2MASS lacks *J* and *H* uncertainties, indicating that these values are likely brightness upper limits.

For the unresolved binary PHα 41, we divide the flux in each band between PHα 41 A and B based on the absolute magnitude–derived K5/K6 flux ratio of Pecaut & Mamajek (2013). This assumes any excess optical or infrared light scales similarly for the two components.

Spectral type assignments are from comparisons to our catalog of main-sequence K- and M-type spectra (see Section 2.1). Corresponding colors and temperatures are assigned from the main-sequence dwarf grid of Pecaut & Mamajek (2013). Though Pecaut & Mamajek (2013) offered a grid specifically for young stars, we opt for their dwarf grid for its $R-I$ colors, currently unavailable in the young star grid. The mismatch in evolutionary stages of the dwarf color grid and young targets may introduce small systematic errors, discussed where encountered.

For each of the following steps, we propagate magnitude uncertainties in the flux regime, where errors are assumed to be Gaussian. Magnitude uncertainties from the empirical data of Pecaut & Mamajek (2013) are roughly 0.001–0.01 mag, and those from Rieke & Lebofsky (1985) are 0.03 mag; both are neglected.

4.2. Veiling Correction

To measure the brightness of the young stars' photospheres and determine their luminosities, we must unveil and deredden the stars. Using veiling values r_{6500} for R and r_{8400} for I, we remove the excess continuum as follows:

$$R_u = R + 2.5\log(1 + r_{6500}), \quad (4)$$

$$I_u = I + 2.5\log(1 + r_{8400}), \quad (5)$$

where R_u and I_u are the unveiled magnitudes. We apply this procedure to the nine PHα stars, for which we have spectroscopically determined veiling and optical photometry. The star CG 30 IRS 4 has measured veiling values but no optical photometry.

Kim et al. (2005) did not measure veiling values. All 10 KWW stars are reportedly weak-line T Tauri stars (Kim et al. 2005), associated with weak or no accretion and veiling. We therefore set the veiling for these stars to zero, but we include a veiling uncertainty of 0.2 in r_{6500} and 0.1 in r_{8400} in case the stars resemble PHα 12, a weak-line T Tauri star with slight veiling. The star IRAS 08159–3543, reportedly a deeply embedded F0–G0 star with broad Hα emission (Neckel & Staude 1995), lacks veiling measurements and optical photometry.

4.3. Extinction Correction

Because the R and I bands dodge the brunt of blue veiling and infrared excess, $R-I$ is considered the most reliable color for determining the visual extinction of young stars (Meyer et al. 1997). For the nine PHα stars and nine KWW stars with optical photometry, we quantify extinction A_V by comparing unveiled $R_u - I_u$ to the intrinsic $(R-I)_{\rm int}$ of Pecaut & Mamajek (2013) and utilizing the extinction relations of Rieke & Lebofsky (1985). The A_V values from this $R-I$ approach range from 0.00 to 2.3 mag. Comparison of Pecaut & Mamajek's (2013) $V-I$ main-sequence colors to young star colors suggests that the $(R-I)_{\rm int}$ we assign will tend to be systematically slightly blue and therefore slightly overestimate extinctions.

For the three stars without optical photometry, CG 30 IRS 4, KWW XRS 9, and IRAS 08159–3543, we derive extinctions

using the classical T Tauri star locus of Meyer et al. (1997) in *JH–HK* color–color space. We solve the locus for extinction A_V,

$$A_V = \frac{0.58(H-K) - (J-H) + 0.52}{1.58A_H/A_V - 0.58A_K/A_V - A_J/A_V}, \quad (6)$$

where $A_J/A_V = 0.282$, $A_H/A_V = 0.175$, and $A_K/A_V = 0.112$ (Rieke & Lebofsky 1985). The resulting A_V values range from 0.0 to 0.99 mag.

This *JH–HK* method does not directly account for veiling or infrared excess and is based predominantly on spectral type M0, with correspondingly red $J-K$ color (Meyer et al. 1997). The extinction of IRAS 08159–3543, with a spectral type between F0 and G0, is likely underestimated. The extinction of CG 30 IRS 4 may also be underestimated, as its J and H magnitudes are only upper limits.

4.4. Bolometric Correction

We estimate each star's apparent bolometric magnitude by adding a spectral type–determined bolometric correction BC_V and intrinsic color $(V-M_\lambda)_{\rm int}$ from Pecaut & Mamajek (2013) to each star's unveiled and dereddened $R_{\rm ud}$ and $I_{\rm ud}$ and dereddened J_d magnitudes. Specifically, for the 18 stars with optical photometry, we define the final apparent bolometric magnitude $m_{\rm bol}$ as the flux-weighted average of the two bolometric magnitudes calculated from $R_{\rm ud}$ and $I_{\rm ud}$. These two bolometric magnitudes are within 0.4 of each other for all 18 stars and identical for 13. For the three stars without optical photometry, we set $m_{\rm bol}$ equal to the bolometric magnitude calculated from J_d. Final apparent bolometric magnitudes for the 21 stars range from 10.90 to 16 mag.

Bolometric magnitude uncertainties range from 0.23 to 2.1 mag. The largest source of uncertainty is, in most cases, the young stars' photometric variability.

4.5. Near-infrared Excess

We quantify young stars' near-infrared excess as $\Delta K = (J–K)_{\rm obs} - (J–K)_{\rm int}$, from observed $J-K$ color versus intrinsic Pecaut & Mamajek (2013) main-sequence $J-K$ color. Near-infrared excesses here range from −0.19 to 1.3 mag (see Table 6). Uncertainties are flux-propagated from the uncertainties in photometry. These excess values appear somewhat correlated with veiling values, and most stars with low veiling have no infrared excess. Our results for the 10 KWW stars corroborate those of Kim et al. (2005), who found that only KWW 873 exhibits an infrared excess. In total, seven of the 21 stars show an infrared excess $\gtrsim$0.1 mag, including CG 30 IRS 4. Because CG 30 IRS 4's J magnitude is an upper limit only, its near-infrared excess may be underestimated.

4.6. Distances from Gaia DR2 Parallaxes and Apparent Associations

Gaia DR2 parallaxes are available for 16 of the 21 stars. We adopt the probabilistically inferred distances d of Bailer-Jones et al. (2018; see Table 6). Eleven *Gaia* DR2 stars within 20.″1 of CG 30, except for PHα 21 with a negative parallax (see Bailer-Jones et al. 2018), appear fairly clustered at a distance of ∼360 pc, especially the six stars PHα 14 and 15 and KWW 464, 598, 1863, and 2205, with distances 354.1–370 pc. Based on these six stars, we define the CG 30 association at an error-weighted-mean distance of 358.1 ± 2.2 pc. This value is similar to the distances to ζ Pup and γ^2 Vel at the heart of the Gum Nebula (Apellániz et al. 2008). In the vicinity of the CG 30 association are eight candidate members, three with positive *Gaia* DR2 parallaxes, one with a negative parallax, and four with none. The three with positive parallaxes are 121–420 pc ahead of or behind the CG 30 association distance. For purposes of calculating luminosity, we assign the four candidate stars without parallaxes the CG 30 association distance, including CG 30 IRS 4, assumed to be inside cometary globule CG 30. We thus suggest that 358.1 ± 2.2 pc is the distance to the entire CG 30/31/38 cometary globule complex. The globules are then 34^{+10}_{-7} pc from ζ Pup and 70^{+12}_{-1} pc from γ^2 Vel.

The star KWW XRS 9 has a distance of 223.3 ± 2.4 pc, somewhat consistent with the CG 30 association, but we exclude the star from candidacy due to kinematics (see Section 5.1.2).

The star PHα 41 lies farther away at 985^{+32}_{-30} pc, which likely places it beyond the Gum Nebula. Negative parallaxes could place PHα 40 and 44 even farther away; however, parallaxes for faint objects at distances $\gtrsim$1 kpc are highly uncertain (Bailer-Jones et al. 2018; Lindegren et al. 2018). The stars PHα 40, 41, 44, and 51, and possibly PHα 34, visually trace a dust lane (Pettersson 1987), and their v_r values agree reasonably well, 29.69–33.69 km s^{-1}. Under the assumption that the young stars tracing the dust lane near PHα 41 are related to PHα 41 (see Section 5.1.2), we group PHα 40, 41, 44, and 51 and assign PHα 51 the distance to PHα 41.

At 153^{+17}_{-14} pc, PHα 34 is apparently a foreground star. The small and very uncertain parallax of IRAS 08159–3543 yields a distance of 2500 pc. It is probably beyond the Gum Nebula.

4.7. Bolometric Luminosity

From $m_{\rm bol}$ and d, we calculate bolometric luminosity L in solar units based on solar bolometric magnitude $M_{\rm bol,\odot} = 4.7554 \pm 0.0004$ mag (Pecaut & Mamajek 2013). Results range from 0.02 to 76 $L_\odot$, with median $L = 0.60$ $L_\odot$ (see Table 6). Flux-propagated bolometric magnitude uncertainties and distance uncertainties are converted to asymmetric luminosity errors. Stars with the largest night-to-night variations in magnitude (PHα 15 and 41) and stars with negative parallaxes (PHα 21, 40, and 44) have the largest luminosity uncertainties. Because our comparisons to a main-sequence color grid cause a slight systematic overestimation of extinction (see Section 4.3), young star luminosities may be systematically high—5.6% on average, 26% at most—based on flux propagation of extinction errors.

4.8. Effective Temperature

We assign young stars' effective temperatures $T_{\rm eff}$ based on their spectral types and the main-sequence grid of Pecaut & Mamajek (2013). Temperatures range from 3100 K–6510 K (see Table 6). For most stars, we take uncertainties as the difference in temperature between the best spectral type and the types 0.5–1 above and below, according to spectral type uncertainty (see Section 3.5). With spectral type range G2–K0 (Kim et al. 2005), KWW 1055 is assigned an intermediate spectral type of G7 with temperature 5530^{+240}_{-250} K. The star IRAS 08159–3543 is assigned a range of spectral types from F0 to G0 and has a corresponding range in temperature (Neckel & Staude 1995).

Though Pecaut & Mamajek (2013) provide pre-main-sequence temperatures, we use their main-sequence temperatures

Table 6
H-R Diagram Parameters

Star Name	A_V (mag)	ΔK (mag)	$m_{\rm bol}$ (mag)	d (pc)	$T_{\rm eff}$ (K)	L ($L_\odot$)	$d_{\rm isoc}$ (pc)
CG 30 Association							
PHα 14	1.0 ± 1.2	−0.04 ± 0.10	13.07 ± 0.53	370^{+100}_{-67}	$3250^{+160}_{-50.}$	$0.65^{+0.48}_{-0.39}$	265
PHα 15	1.1 ± 4.3	0.09 ± 0.11	12.6 ± 1.9	$354.4^{+4.7}_{-4.5}$	$3200.^{+50.}_{-100}$	0.9 ± 1.6	191
KWW 464	0.00 ± 0.96	−0.19 ± 0.11	13.88 ± 0.39	$360.5^{+4.1}_{-4.0}$	$3410.^{+90.}_{-160}$	0.29 ± 0.11	500
KWW 598	2.25 ± 0.94	0.04 ± 0.11	13.49 ± 0.38	$354.1^{+9.3}_{-8.8}$	$3550^{+100}_{-50.}$	0.40 ± 0.14	482
KWW 1863	0.52 ± 0.92	0.05 ± 0.13	12.60 ± 0.37	$356.9^{+4.0}_{-3.9}$	$3700.^{+75}_{-50.}$	0.92 ± 0.32	360
KWW 2205	0.00 ± 0.93	−0.14 ± 0.10	13.74 ± 0.38	$365.5^{+7.2}_{-7.0}$	$3200.^{+50.}_{-100}$	0.34 ± 0.12	327
CG 30 Association Candidates with *Gaia* DR2 Distances							
PHα21	0.3 ± 1.3	−0.07 ± 0.10	13.77 ± 0.57	3800^{+2500*}_{-1500}	$3100^{+100}_{-70.}$	36^{+51}_{-34}	280
KWW 873	0.55 ± 0.92	0.11 ± 0.10	12.34 ± 0.37	237^{+14}_{-12}	4050^{+150}_{-200}	0.52 ± 0.19	424
KWW 1637	0.00 ± 0.92	0.05 ± 0.10	11.15 ± 0.37	780^{+670}_{-250}	4200^{+250}_{-150}	17^{+29}_{-12}	282
KWW 1953	0.30 ± 0.93	−0.18 ± 0.10	13.26 ± 0.38	456^{+55}_{-45}	$3410.^{+90.}_{-160}$	$0.83^{+0.35}_{-0.33}$	376
CG 30 Association Candidates Assigned CG 30 Association Distance							
PHα 12	0.35 ± 0.67	−0.01 ± 0.10	13.15 ± 0.29	[358.1 ± 2.2]	$3410.^{+90.}_{-160}$	0.56 ± 0.15	358
KWW 1055	0.97 ± 0.92	0.06 ± 0.11	13.33 ± 0.37	[358.1 ± 2.2]	5530^{+240}_{-250}	0.48 ± 0.16	2776
KWW 1302	0.00 ± 0.92	−0.05 ± 0.14	13.34 ± 0.37	[358.1 ± 2.2]	$3200.^{+50.}_{-100}$	0.47 ± 0.16	271
CG 30 IRS 4	0.99	0.61	16	[358.1 ± 2.2]	3850^{+200}_{-75}	0.04	1882
Stars near PHα 41							
PHα 40	1.55 ± 0.53	0.05 ± 0.10	14.40 ± 0.23	4400^{+2500*}_{-1600}	3775 ± 75	$27^{+31}_{-20.}$	876
PHα 41 A	2.0 ± 5.0	0.52 ± 0.10	14.6 ± 2.1	$985^{+32}_{-30.}$	4450^{+170}_{-250}	1.1 ± 2.2	1762
PHα 41 B	0.7 ± 5.0	0.52 ± 0.10	16.3 ± 2.1	$985^{+32}_{-30.}$	4200^{+250}_{-150}	0.23 ± 0.45	3034
PHα 44	1.46 ± 0.65	0.18 ± 0.12	14.29 ± 0.28	7000^{+2800*}_{-2000}	4450^{+170}_{-250}	76^{+64}_{-48}	1526
PHα 51	0.0 ± 1.3	0.29 ± 0.11	15.95 ± 0.55	$[985^{+32}_{-30.}]$	3775 ± 75	0.32 ± 0.17	1789
Other Stars							
PHα 34	2.3 ± 1.9	0.34 ± 0.12	14.74 ± 0.85	155^{+18}_{-15}	4050^{+150}_{-200}	0.02 ± 0.02	1283
KWW XRS 9	0.0 ± 1.1	−0.00 ± 0.10	10.90 ± 0.31	223.3 ± 2.4	$5660.^{+20.}_{-70.}$	1.73 ± 0.50	1073
IRAS 08159–3543	0.0	1.3	14	2500^{+2200}_{-1200}	6510^{+690}_{-590}	13	9536

Note. Distances and temperatures in brackets are assigned according to a possible physical association with another star or stars (see text). Distances followed by asterisks * are derived from negative parallaxes (see Bailer-Jones et al. 2018).

(This table is available in machine-readable form.)

to maintain consistency with our use of their main-sequence $R-I$ colors. Consequent systematic differences in temperature range from −130 to +310 K for G-, K-, and M-type stars. These differences are comparable to uncertainties from determining spectral type and, on average, may overestimate temperature by 100 K.

4.9. Masses and Ages from an H-R Diagram

We plot the 21 stars' L versus T on an H-R diagram, along with the mass tracks and isochrones of Baraffe et al. (2015) for comparison (Figure 6). All temperatures, photometric properties, and distances are listed in Table 6, grouped by possible associations.

Most of the stars apparently have masses $<1.0\,M_\odot$, as expected of K- and M-type young stars. Of the 14 CG 30 association stars and candidates, 12 map to an age of near or less than 1 Myr. Isochrones from Baraffe et al. (2015) and MESA (Figure 6) and from Baraffe et al. (1998) suggest an age of ∼0.5 Myr, while isochrones from Siess et al. (2000) and Feiden (2016) suggest an age of ∼1 Myr. In all scenarios, the majority of stars near CG 30 appear to belong to a very young, coeval population aged $\lesssim$1 Myr. The G-type star KWW 1055, as well as kinematically disqualified KWW XRS 9, might be older, perhaps 50–100 Myr, field stars, as Kim et al. (2005) suggested.

The remaining CG 30 association star, CG 30 IRS 4 itself, appears very underluminous compared to other CG 30 association members and candidates. Its position near the zero-age main sequence is inconsistent with its embedded state, strong lithium absorption, and signatures of accretion. We suspect this stems from the scattering of the star's light, consistent with its spatially extended appearance (see Section 2.1), and the underestimation of its extinction ($A_V = 0.99$). Photospheres revealed through scattered light (e.g., HL Tau, HV Tau C; White & Ghez 2001) are artificially blue, causing the extinction to be underestimated. The star's J and H magnitudes are also only upper limits.

The star PHα 34 also sits below the zero-age main sequence on the H-R diagram. This star exhibits heavy veiling, which can be associated with underestimated luminosity (White & Ghez 2001).

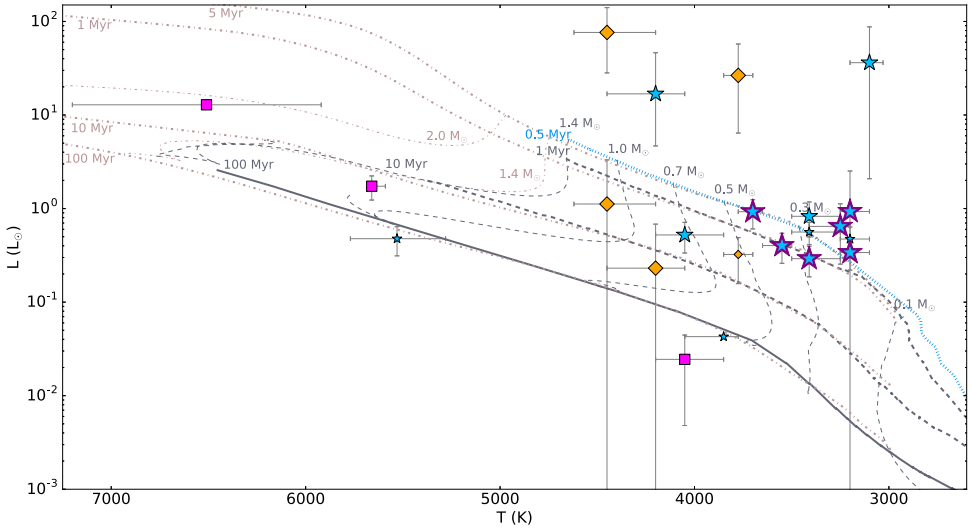

Figure 6. We plot luminosity vs. temperature for the 14 CG 30 association stars and candidates (blue star symbols), the five stars near PHα 41 (orange diamonds), and the three other stars (magenta squares). The six defining members of the CG 30 association are outlined in purple. *Gaia* DR2 distances are incorporated where available and represented with large symbols. Stars assigned distances for possible relation to the CG 30 association or PHα 41 (see text and Table 6) are represented with small symbols. Mass tracks and isochrones are from Baraffe et al. (2015; dotted and dashed gray lines; mass $\leqslant$1.4 $M_{\odot}$) and supplemented with MESA (dotted–dashed pale pink-gray lines; mass >1.4 $M_{\odot}$; Choi et al. 2016; Dotter 2016; Paxton et al. 2011, 2013, 2015). The Baraffe et al. (2015) 0.5 Myr isochrone (blue dotted line) passing through the CG 30 association stars is used to calculate isochrone distances (see Table 6).

The stars PHα 21, 40, and 44 and KWW 1637 appear markedly overluminous, 12–230 times brighter that the 1 Myr isochrone at their temperatures. The distance 780^{+670}_{-250} pc to KWW 1637 is relatively uncertain and may be overestimated. The negative-parallax distances to PHα 21, 40, and 44 may be especially overestimated, feasibly by a factor of 4–10, considering *Gaia* DR2's drop in reliability past 1 kpc values (Bailer-Jones et al. 2018; Lindegren et al. 2018).

The broad Hα emissions, Li absorptions, veiling values, and positions on the H-R diagram confirm that most of the stars studied here are young. Many of the CG 30 association stars and candidates sit at or above the 1 Myr isochrone. If we assume an age of 0.5 Myr, we can use the 0.5 Myr isochrone to determine an isochrone distance $d_{\rm isoc}$ for the given $T_{\rm eff}$ and $m_{\rm bol}$. This allows us to estimate distances without *Gaia* DR2 data and test results where *Gaia* DR2 data are available.

Isochrone distances vary from 191 to 9536 pc (see Table 6). Values for the 14 CG 30 association members and candidates hover around a median of 360 pc, suggesting that the 14 stars are indeed very young, inside the Gum Nebula, and possibly related to each other. Isochrone distances for stars spatially near PHα 41 are 109–804 pc off of PHα 41's distance, much shorter than the Bailer-Jones et al. (2018) estimates. The isochrone distance to PHα 34 (1283 pc) is also more similar to PHα 41's *Gaia* DR2 distance (985^{+32}_{-30} pc) than PHα 34's *Gaia* DR2 distance (155^{+18}_{-15} pc). Isochrone distances for PHα 41 itself, KWW XRS 9, and IRAS 08159–3543 are vast overestimates. The stars near PHα 41 and other stars are not likely related to CG 30.

5. Discussion

We have assembled stellar properties of 21 stars at the northern edge of the Gum Nebula. The youth and proximity of a subset of these stars, specifically the CG 30 association stars and candidates studied by Pettersson (1987) and Kim et al. (2005), strongly suggest that they formed as one population $\lesssim$1 Myr ago.

5.1. Kinematics

Radial velocities coupled with *Gaia* DR2 proper motions allow us to investigate the 3D motions of stars in this region (see Figure 7). We assemble v_r for the nine PHα stars and CG 30 IRS 4 from our own spectroscopic analysis. For the 10 KWW stars and IRAS 08159–3543, we convert the local standard-of-rest velocities of Bronfman et al. (1996) and Kim et al. 2005) to v_r by adding 17.3 km s^{-1} to each. *Gaia* DR2 and Choudhury & Bhatt (2009) provide proper motions for 18 of the 21 stars studied here (see Table 7).

5.1.1. CG 30 Association

Radial velocities, available for 13 of the 14 CG 30 association stars and candidates, support the proposition of Kim et al. (2005) that several stars near CG 30 are dynamically related. A dispersion of $\leqslant$5 km s^{-1} is typical of open clusters (Soubiran et al. 2018), while 1–2 km s^{-1} is typical of young open clusters. The six defining members of the CG 30 association recede at v_r = 21.5–26.77 km s^{-1}, with error-weighted mean 22.3 km s^{-1} and sample standard deviation 2.0 km s^{-1}. Including all candidates barely increases the v_r range to 20.0–26.77 km s^{-1}, with error-weighted mean 23.1 km s^{-1} and sample standard deviation 1.9 km s^{-1}. Thus, v_r data support the grouping of 13 of the CG 30 association members and candidates, including KWW 1055, which, if part of the CG 30 association, may be younger than it appears on the H-R diagram (Figure 4.9). Though KWW 1055 lies below the main sequence, it shows undepleted Li I λ6708 (Kim et al. 2005).

The gas of cometary globule CG 30 has v_r = 22.8 km s^{-1} (Zealey et al. 1983; De Vries et al. 1984), well within the range of the CG 30 association stars, as expected (Kim et al. 2005). This further supports ascribing the CG 30 association distance to the cometary globule itself.

Gaia DR2 and Choudhury & Bhatt (2009) provide proper motions μ_α in R.A. and μ_δ in decl. for 11 of the 14 CG 30 association and candidate stars. The six tight CG 30 association members' proper motions agree well, with $\mu_\alpha = -7.89$ to

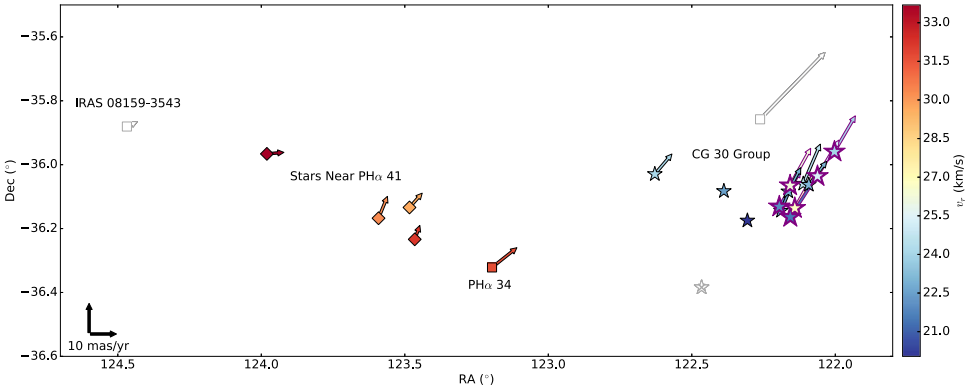

Figure 7. We plot the R.A. and decl. of 21 stars, with the color bar showing v_r and arrows indicating proper motion in mas yr^{-1}, scaled up by a factor of 10 in the figure (see proper-motion scale in black in the lower left corner). Star symbols mark CG 30 association stars and candidates, with the six CG 30 association members outlined in purple. Diamonds mark the four stars near PHα 41. Other stars are represented by squares. The v_r color legend extends over the range of interest from 20.0 to 33.69 km s^{-1}. Stars with v_r outside this range have no color. The star KWW 1302 with no v_r bears an X. At least 13 of the stars spatially near CG 30 may be dynamically related. The relation of the stars near PHα 41 is weakly suggested.

Table 7
Proper Motions and Radial Velocities

Star Name	v_r (km s^{-1})	μ_α (mas yr^{-1})	μ_δ (mas yr^{-1})
	CG 30 Association		
PHα 14	26.77 ± 0.89	−7.32 ± 0.90	11.72 ± 0.90
PHα 15	21.99 ± 0.20	−7.579 ± 0.068	11.451 ± 0.067
KWW 464	24.0 ± 3.0[a]	−7.510 ± 0.051	11.603 ± 0.051
KWW 598	21.5 ± 3.0[a]	−7.89 ± 0.13	10.98 ± 0.13
KWW 1863	26.2 ± 3.0[a]	−7.400 ± 0.056	12.025 ± 0.056
KWW 2205	25.3 ± 3.0[a]	−7.728 ± 0.093	11.675 ± 0.087
	CG 30 Association Candidates with *Gaia* DR2 Distances		
PHα 21	24.12 ± 0.21	−6.26 ± 0.48	6.62 ± 0.57
KWW 873	22.3 ± 3.0[a]	−4.19 ± 0.38	9.15 ± 0.39
KWW 1637	22.8 ± 3.0[a]	−4.55 ± 0.77	7.81 ± 0.78
KWW 1953	24.5 ± 3.0[a]	−6.14 ± 0.39	12.79 ± 0.40
	CG 30 Association Candidates Assigned CG 30 Group Distance		
PHα 12	23.07 ± 0.15	−6.5 ± 4.8[b]	7.7 ± 4.7[b]
KWW 1055	20.0 ± 3.0[a]	…	…
KWW 1302	…	…	…
CG 30 IRS 4	22.5 ± 2.0	…	…
	Stars near PHα 41		
PHα 40	32.16 ± 0.29	−1.95 ± 0.43	4.76 ± 0.51
PHα 41	29.69 ± 0.41[c]	−4.738 ± 0.050	4.791 ± 0.051
PHα 44	30.29 ± 0.15	−3.27 ± 0.29	7.23 ± 0.31
PHα 51	33.69 ± 0.44	−6.4 ± 4.8[b]	0.5 ± 4.6[b]
	Other Stars		
PHα 34	31.65 ± 0.29	−9.0 ± 1.1	6.4 ± 1.1
KWW XRS 9	−74.1 ± 3.0[a]	−22.948 ± 0.072	21.203 ± 0.077
IRAS 08159–3543	49.2	−4.03 ± 0.91	1.67 ± 0.88

Notes.
[a] Kim et al. (2005).
[b] Choudhury & Bhatt (2009).
[c] The reported v_r for PHα 41 is the systemic v_r of the binary (see text).
(This table is available in machine-readable form.)

−7.32 and $\mu_\delta = 10.98$–12.025 mas yr^{-1}. This yields error-weighted means and sample standard deviations $\mu_\alpha = -7.53 \pm 0.19$ mas yr^{-1} (-12.79 ± 0.32 km s^{-1} at distance 358.1 pc) and $\mu_\delta = 11.67 \pm 0.32$ mas yr^{-1} (19.82 ± 0.54 km s^{-1}). Including all candidates results in similar averages, $\mu_\alpha = -7.5 \pm 1.2$ mas yr^{-1} (-12.7 ± 2.0 km s^{-1}) and $\mu_\delta = 11.6 \pm 2.0$ mas yr^{-1} (19.7 ± 3.4 km s^{-1}), supporting the grouping of 11 of the CG 30 association members and candidates.

When the range of velocities in each direction (radial, R.A., and decl.) is small, as here, the coordinate system can be assumed to be roughly Cartesian (Kuhn et al. 2019). Following the example of Kuhn et al. (2019), we define a 1D velocity dispersion σ_{1D} from the mean variance of the three orthogonal dispersions,

$$\sigma_{1D}^2 = \frac{\sigma_{v_r}^2 + \sigma_{\mu_\alpha}^2 + \sigma_{\mu_\delta}^2}{3}, \quad (7)$$

where σ_{v_r}, σ_{μ_α}, and σ_{μ_δ} are the sample standard deviations of v_r, μ_α, and μ_δ, respectively, all in km s^{-1}. The 28 clusters examined by Kuhn et al. (2019) have $\sigma_{1D} = 0.8$–2.8 km s^{-1} and tend to expand over time. The tight CG 30 association members have $\sigma_{1D} = 1.2$ km s^{-1}, and the association plus candidates have 2.5 km s^{-1}. Both values fall within the range of Kuhn et al. (2019).

We conclude that PHα 12, 14, 15, and 21; KWW 464, 598, 873, 1055, 1302, 1637, 1863, 1953, and 2205; and CG 30 IRS 4 all constitute the CG 30 association near cometary globule complex CG 30/31/38 at a distance of 358.1 ± 2.2 pc. Our findings confirm Kim et al. (2005) and recommend adding PHα 21, KWW 1055, and CG 30 IRS 4 to the association.

5.1.2. Stars outside the Gum Nebula

Though possibly inside the Gum Nebula at 223.3 ± 2.4 pc, KWW XRS 9 has velocities inconsistent with the CG 30 association ($v_r = -74.1 \pm 3.0$ km s^{-1}, $\mu_\alpha = -22.948 \pm 0.072$ mas yr^{-1}, and $\mu_\delta = 21.203 \pm 0.077$ mas yr^{-1}) and may be a young foreground star.

The v_r of the four stars near PHα 41, as well as PHα 34, appear to match, 29.69–33.69 km s^{-1}. The proper motions of PHα 34, 40, 41, 44, and 51 are also somewhat similar; however, their σ_{1D} is high at 8.0 km s^{-1}. Age, position, and kinematics weakly suggest that the stars near PHα 41 may be related.

The star IRAS 08159–3543 appears not to be kinematically associated with any other stars in our sample (see Table 7). The star was ascribed an aberrantly high luminosity of 24,000 $L_\odot$ by Neckel & Staude (1995), versus our much more modest estimate of 13 $L_\odot$. We use a smaller distance (2500 pc) than the Neckel & Staude (1995) estimate of 4300 pc, smaller even than their lower limit of 3400 pc assumed for RCW 19, although the parallax of IRAS 08159–3543 is quite uncertain. The high luminosity estimate of Neckel & Staude (1995) stems chiefly from their large assigned extinction of $A_V = 43$ that is difficult to reconcile with IRAS 08159–3543's optical spectrum. The star nevertheless appears to be young and of intermediate mass, with a strong near-infrared excess and a wind (Neckel & Staude 1995).

5.2. Star Formation in Cometary Globules

The Gum Nebula hosts at least 32 cometary globules (Sridharan 1992; Kim et al. 2005), and at least 16 are associated with IRAS point sources (Bhatt 1993). Three (Bernes 135 = NX Pup A in CG 1, PHα 92 = Wray 220 in CG 22, and CG 30 IRS 4 in CG 30) are spectroscopically confirmed young stars associated with cometary globule heads. Acted on by external radiation, cometary globules are theorized to host an enhanced rate of star formation and possibly higher accretion rates (Bhatt 1993; Maheswar & Bhatt 2008). Bhatt (1993) found that the cometary globules of the Gum Nebula contain a surface density of young star–like IRAS sources 3–12 times higher than a control group of neighboring dark clouds, which, combined with their compact size, suggests a star formation efficiency of up to ∼30% (Bhatt 1993). Globules may preferentially form low-mass, isolated stars like the Sun (Bhatt 1993; Kim et al. 2005; Walch et al. 2013). It is reasonable to assume that several young stars in the Gum Nebula may have originated inside cometary globules, perhaps a few stars per head (Pettersson 1987; Bhatt 1993; Kim et al. 2005).

Of the few specimens observed, we see a range of spectral types and masses. Bernes 135 at the edge of CG 1 is thought to be an F1–F2-type star 1 Myr of age and mass 2.5–3.0 $M_\odot$, with luminosity 27–30 $L_\odot$ if at a Gum Nebula distance of 350 pc (Reipurth 1983). The star may have two companions: NX Pup B of type F5–G8 with luminosity 5.4–11 $L_\odot$ and NX Pup C of type M0.5–M1.5 with luminosity 0.27–0.51 $L_\odot$ (Pettersson 2007). Optically revealed PHα 92 in front of CG 22 is a T Tauri star of type K2–K3 with luminosity 8.9 $L_\odot$ (Sahu & Sahu 1992). Outside the Gum Nebula, globule IC 1396A hosts a T Tauri star of type M2 and a protostar (Sicilia-Aguilar et al. 2013).

The star CG 30 IRS 4 has been previously studied for signs of stellar activity. The infrared source helps power the Herbig–Haro object HH 120 (Persi et al. 1994; Pettersson 2007; Chen et al. 2008; Kajdič et al. 2010) and overlaps the submillimeter source CG 30 SMM-N associated with the large bipolar jet HH 950 (Kajdič et al. 2010). The complexity of the Herbig–Haro objects indicates that the star is part of a wide binary system (Pettersson 2007; Chen et al. 2008; Kajdič et al. 2010). Our high-dispersion spectroscopy shows that CG 30 IRS 4 is a low-mass star of type M0 with moderate veiling of 0.86 near 6500 Å and 0.15 near 8400 Å. It is definitely young, with a lithium equivalent width of 0.47–0.67 Å. Kim et al. (2005) proposed that the object is as young as just 10^5 yr. Strong 1.3 mm emission and NH_3 observations suggest that the star is embedded in a dense cloud core of size 0.14 pc (at a distance of 358.1 pc) and mass 8 $M_\odot$. Chen et al. (2008) suggested an outflow mass of 1.4 $M_\odot$. The star's luminosity may be as high as 13.6 ± 0.8 $L_\odot$ (Pettersson 2007; Chen et al. 2008).

The star CG 30 IRS 4 has the lowest v_{rot} sin(i) of our sample, 6.3 ± 0.2 km s^{-1}. Though embedded, the star seems to have already dissipated much of the angular momentum of its formation, suggesting that this may happen during the embedded stage (White & Hillenbrand 2004). Rotation speed may then hold fairly constant until dissipation of the circumstellar disk (Gallet & Bouvier 2013). With its relatively slow v_{rot} sin(i), defined photosphere, strong lithium absorption, weak but present Hα emission, and moderate veiling, CG 30 IRS 4 resembles the optically revealed T Tauri stars of the CG 30 association. It may essentially be an embedded T Tauri star. Perhaps stars evolve T Tauri properties (e.g., photosphere, disk) before emerging from a cloud.

Considering the 14 CG 30 association stars' proximity to actively star-forming cometary globules, it is possible that all formed inside cometary globules (Kim et al. 2005). The 14 T Tauri stars do not appear to differ from low-mass T Tauri stars formed by the traditional collapse of a large molecular cloud. While FUV radiation forms cometary globules that appear to host enhanced, isolated, low-mass star formation rates (Bhatt 1993; Walch et al. 2013), the radiation may not penetrate deep enough to affect the star formation process itself (Elmegreen 2011; Paron et al. 2015).

5.3. Young Star Evolution in a Moderate Radiation Environment

Once a star emerges from its formative gas and dust, external radiation from any nearby OB stars can act on the young star's protoplanetary disk. Disks in the fiery heart of the ONC, the proplyds, are visibly elongated (e.g., O'Dell et al. 1993). Even from tens of pc away, the light from OB stars may disperse a young star's protoplanetary disk faster than normal and disrupt accretion (Walter et al. 1988; Hillenbrand 2005; Kim et al. 2005; Eisner et al. 2008). If the moderate radiation environment of the Gum Nebula is affecting young stars' disks there, then we should see a smaller ratio of accretors to nonaccretors in the CG 30 association than in more quiescent regions of similar age (e.g., Tau-Aur). Mohanty et al. (2005) calculated the accretor fraction as $N_{\rm acc}/N_{\rm tot}$, where $N_{\rm acc}$ is the number of classical T Tauri stars with $W_{10} > 200\,{\rm km\,s^{-1}}$, and $N_{\rm tot}$ is the total number of T Tauri stars both weak and classical. The accretor fractions for various star-forming regions range from $59\% \pm 16\%$ for the 1–3 Myr Tau-Aur to $2\% \pm 2\%$ for the 10 Myr NGC 7160 (see Table 8).

To the Mohanty et al. (2005) compilation, we add accretor fractions from Mortier et al. (2011), who distinguished accretors from nonaccretors using $W_{10}({\rm H}\alpha)$ and the same prescription as Mohanty et al. (2005); Sicilia-Aguilar et al. (2005b, 2005a, 2013), Fang et al. (2013), Biazzo et al. (2014), and Briceño et al. (2019), who used $W_{10}({\rm H}\alpha)$ and the prescription of White & Basri (2003); and Hernández et al. (2007), who distinguished accretors from nonaccretors photometrically based on thick versus thin disks. Assembling accretor fractions from multiple sources measured in different ways inevitably introduces bias. However, there is no established way of measuring accretor fraction yet, and synthesizing results provides us with useful context (see also Table 2 in Fedele et al. 2010). In Table 8, we group clusters by environment: quiescent (no cometary globules or OB associations) versus irradiated (present cometary globules or OB associations). The quiescent clusters ρ Oph, Tau-Aur, Lup, IC 348, Cha I, and TW Hyd tend to have higher accretor fractions (15%–59%), whereas the clusters L1641, L1615/1616, Tr 37, NGC 1977/1980, σ Ori, Upper Sco, and NGC 7160 near cometary globules or OB associations tend to have lower accretor fractions (2%–40%). Accretor fractions generally decline with age, which dominates after 5 Myr (Mohanty et al. 2005; Fedele et al. 2010).

The ONC, despite containing proplyds and several massive stars, has a relatively high accretor fraction inconsistent with other irradiated clusters of similar age ($57\% \pm 5\%$ versus 28%–40%). This may be due to the region's complex and recent star formation history (Winter et al. 2019).

Of the 14 CG 30 association stars and candidates, three are classical T Tauri stars by our criterion of $W_{10}({\rm H}\alpha) > 270\,{\rm km\,s^{-1}}$, and 11 are weak-line. The star CG 30 IRS 4, though classified among the weak-line stars, is embedded, veiled, and likely still accreting. The CG 30 association then has an accretor fraction of $29\% \pm 14\%$ (4/14). By the criterion of Mohanty et al. (2005), the accretor fraction would be $36\% \pm 16\%$ (5/14). Either fraction is low for the CG 30 association's age of $\lesssim$1 Myr, as Kim et al. (2005) suggested. The similarly aged Tau-Aur and ρ Oph clusters have accretor fractions about twice as high. The CG 30 association's accretor fraction is more consistent with irradiated clusters than quiescent clusters.

The CG 30 association measurement is subject to low number statistics, although the association itself appears sparse, with only six additional potential members since being found via *Gaia* DR2 (A. C. Yep and R. J. White 2020, in preparation). It is also worth considering selection biases. Young stars identified via broad Hα emission (Pettersson 1987; Neckel & Staude 1995) tend to be classical T Tauri stars, whereas young stars identified via X-ray luminosity (Kim et al. 2005) tend to be weak-line T Tauri stars. Using a dual identification approach, as here, has provided the most comprehensive membership lists in comparison star-forming regions (e.g., Cohen & Kuhi 1979 and Neuhäuser et al. 1995 for Tau-Aur). The greater distance to CG 30 compared to these other regions may bias against finding X-ray-bright weak-line T Tauri stars, which, if present, would further reduce the accretor fraction.

Table 8
Accretor Fractions of Star-forming Regions

Region	Age (Myr)	$N_{\rm acc}/N_{\rm tot}$	%
	Quiescent		
ρ Oph	<1[a,c]	10/20[c]	50 ± 16
Tau-Aur	1–3[j,k]	42/71[c]	59 ± 9
Lup	1–3[j,k]	25/45[g]	56 ± 11
IC 348	2–3[j,k]	29/87[c]	33 ± 6
Cha I	2–3[j,k]	28/63[c]	44 ± 8
TW Hyd	10[a,c]	⋯	$\sim$15[c]
	Irradiated		
CG 30	$\lesssim$1	4/14	29 ± 14
L1641	0.1–3[f,h]	159/450[h]	35 ± 3
ONC	0.8–3[l]	136/237[d]	57 ± 5
L1615/1616	1–3[a,i]	15/54[i]	28 ± 7
Tr 37	1–4[b,d]	46/116[d]	40 ± 5
NGC 1977/1980	2–4[a,b,m]	63/222[m]	28 ± 4
σ Ori	3–5[j,k]	⋯	33.9 ± 3.1[e]
Upper Sco	5–10[j,k]	12/170[c]	7 ± 2
NGC 7160	10[b,d]	1/55[d]	2 ± 2

Notes.
[a] Baraffe et al. (1998).
[b] Siess et al. (2000).
[c] Mohanty et al. (2005).
[d] Sicilia-Aguilar et al. (2005a, 2005b, 2013).
[e] Hernández et al. (2007).
[f] Dotter et al. (2008).
[g] Mortier et al. (2011).
[h] Fang et al. (2013).
[i] Biazzo et al. (2014).
[j] Baraffe et al. (2015).
[k] Cazzoletti et al. (2019).
[l] Winter et al. (2019).
[m] Briceño et al. (2019).

(This table is available in machine-readable form.)

6. Summary

We study 21 young stars near CG 30 and RCW 19 to investigate whether these stars are related to each other and how the Gum Nebula's moderate radiation environment ($G_0 = 6.6^{+3.2}_{-2.7}$) may be affecting them. We have observed nine stars from Pettersson (1987) and CG 30 IRS 4 itself using high-dispersion ($R \sim 34{,}000$) spectroscopy and gathered photometry for all 21 young stars from the literature (2MASS; Pettersson 1987; Neckel & Staude 1995; Kim et al. 2005).

1. The spectral types of the nine Pettersson (1987) stars and CG 30 IRS 4 range from M4.5 to K5.
2. The nine Pettersson (1987) stars and CG 30 IRS 4 show undepleted Li λ6708, Hα 10% widths of 225–621 km s^{-1}, and veiling. Eight of the 10 are classical T Tauri stars. Three of the stars associated with CG 30 are classical T Tauri stars.
3. The projected rotational velocities of the 10 young stars are 6.3–27.8 km s^{-1}. The lowest is that of CG 30 IRS 4.
4. The star CG 30 IRS 4 inside the cometary globule appears to be an embedded T Tauri star. Though its Hα 10% width (225 km s^{-1}) falls below the classical T Tauri star limit, it is embedded, exhibits moderate veiling, and is probably still accreting.
5. By youth ($\lesssim$1 Myr), distance (358.1 $\pm$ 2.2 pc), and kinematics (radial velocity 23.1 $\pm$ 1.9 km s^{-1}, proper motions -7.5 ± 1.2 mas yr^{-1} in R.A. and 11.6 ± 2.0 mas yr^{-1} in decl., and 1D dispersion 2.5 km s^{-1}), 14 stars near CG 30 are likely related to each other and the CG 30/31/38 cometary globule complex. This is the CG 30 association.
6. The CG 30 association has an accretor fraction of 29% $\pm$ 14%, which is low compared to young quiescent clusters but consistent with young irradiated clusters.

A.C.Y. and R.J.W. thank L.A. Hillenbrand for her help in initiating this work. Support was provided by NSF AAG grant 1517762. We thank Keck Observatory for use of its cutting-edge facilities and the indigenous people of Hawaii for the opportunity to observe the stars from the peak of Maunakea. This publication makes use of data products from the Two Micron All Sky Survey, which is a joint project of the University of Massachusetts and the Infrared Processing and Analysis Center/California Institute of Technology, funded by the National Aeronautics and Space Administration and the National Science Foundation. This work has made use of data from the European Space Agency mission *Gaia* (https://www.cosmos.esa.int/gaia), processed by the *Gaia* Data Processing and Analysis Consortium (DPAC; https://www.cosmos.esa.int/web/gaia/dpac/consortium). Funding for the DPAC has been provided by national institutions, in particular the institutions participating in the *Gaia* Multilateral Agreement. Thank you to W. Fischer, L. A. Hillenbrand, and the referee for providing such thorough, helpful feedback on A.C.Y.'s first paper. Finally, A.C.Y. specially thanks R. C. Marks, whose unflagging love and support have made this research project possible.

Facility: Keck:I (HIRES).

Appendix
Calculation of G_0

To estimate the FUV radiation factor G_0 (Habing 1968; Winter et al. 2018), we model ζ Pup, γ^2 Vel, and the Vela XYZ progenitor using the Castelli & Kurucz (2004) model atmospheres of O-type dwarfs with solar metallicity. Taking the stars' distances from Earth into account, we scale the model fluxes to match the stars' observed *UBV* magnitudes (see Table 9). This calibrates each star's absolute brightness. We then scale the flux again based on each star's distance from CG 30. We integrate each star's scaled flux over the wavelength range 912–2400 Å for individual G_0. Finally, we sum the three stars' G_0 values and incorporate a relatively small contribution from B stars in Vela OB2. Uncertainties in G_0 stem chiefly from uncertainties in distances to ζ Pup, γ^2 Vel, and Vela XYZ. Within the stars' distance uncertainties, we calculate a maximum G_0 closest to CG 30 and a minimum G_0 farthest from CG 30. The total $G_0 = 6.6^{+3.2}_{-2.7}$.

The Wolf–Rayet star of binary γ^2 Vel is approximated as an O-type dwarf with $T_{\rm eff} = 50{,}000$ K, the hottest model available from Castelli & Kurucz (2004). De Marco & Schmutz (1999) and De Marco et al. (2000) found a primary-to-total flux ratio at 4700 Å $f(O)_{4700}/f(O+WR)_{4700} = 0.795$. From this, we derive *UBV* flux ratios of 0.786, 0.795, and 0.801, respectively, and divide dereddened *UBV* magnitudes between the primary and secondary accordingly. We scale each component model to its set of *UBV* magnitudes and sum the results for γ^2 Vel's G_0 of $2.0^{+0.1}_{-0.8}$.

Vela XYZ likely resulted from a Type 1a or 1b supernova, entailing a massive progenitor (Reipurth 1983). We crudely substitute a star like ζ Pup at the location of Vela XYZ, which, having exploded just 11,000 yr ago (Reipurth 1983), presumably shone on the CG 30 stars during most of their existence.

To quantify the B-type star contribution to G_0, we derive a G_0 versus *Gaia* color *BP*−*RP* relation, find a *BP*−*RP* limit for B-type stars, and tally the B-type stars in Vela OB2 using our *BP*−*RP* limit and the catalog of Cantat-Gaudin et al. (2019). From 15 field B-type stars with *Gaia* DR2 data and known temperatures from Soubiran et al. (2016) placed at the location of γ^2 Vel, we calculate their G_0 and fit a second-degree polynomial to $\log(G_0)$ versus *BP*−*RP*. From a broader sample of 200 field B-type stars with *Gaia* DR2 data and known spectral types, we ascertain that the latest B-type stars have flux-mean $BP - RP = -0.003$ mag. We find 64 stars in Vela OB2 that have $BP - RP < -0.003$ mag. Using our $\log(G_0)$ versus *BP*−*RP* relation, we calculate a Vela OB2 B-type star G_0 contribution of 0.3. A finer calculation is possible with available *Gaia* DR2 data but would be nontrivial, as Vela OB2 has multiple components (Cantat-Gaudin et al. 2019).

We calculate G_0 only from the local O stars and the B stars of Vela OB2. The contribution from a late B star in Vela OB2 is already small, $G_0 \sim 0.002$. The contribution from the G star KWW 1055 within the CG 30 cluster is negligible, $G_0 < 10^{-5}$.

We extrapolate from current G_0 and the O-type stars' radial velocities and proper motions to estimate G_0 at CG 30 1 Myr ago. Runaway ζ Pup had a larger separation from CG 30 (79^{+17}_{-16} pc versus 34^{+10}_{-7} pc), whereas γ^2 Vel had a smaller separation (62^{+6}_{-14} pc versus 70^{+12}_{-1} pc). Holding G_0 from Vela XYZ and Vela OB2 constant and neglecting the stars' luminosity changes due to stellar evolution, we find that G_0 at CG 30 was $4.1^{+1.7}_{-1.8}$ 1 Myr ago, about two-thirds of today's value.

Table 9
Hot Star Parameters

Star Name	$T_{\rm eff}$ (K)	U (mag)	B (mag)	V (mag)	A_V (mag)	d (pc)	r ($R_\odot$)	v_r (km s^{-1})	μ_α (mas yr^{-1})	μ_δ (mas yr^{-1})	G_0
ζ Pup	39000[i]	0.89[i]	1.98[i]	2.25[i]	0.13[d]	335^{+12}_{-11}[e]	16[f]	-23.90 ± 2.9[g]	-29.71 ± 0.08[h]	16.68 ± 0.09[h]	$3.7^{+2.7}_{-1.6}$
γ^2 Vel	35000, 57000[a]	0.64[c]	1.58[c]	1.83[c]	0.51[d]	349^{+44}_{-35}[e]	$18.7^{+2.3}_{-1.9}$, 3.2[a]	15.0 ± 3.1[g]	-6.07 ± 0.30[h]	10.43 ± 0.32[h]	$2.0^{+0.1}_{-0.8}$
Vela XYZ	...	...	...	...	...	294^{+76}_{-50}[b]	...	...	...	...	$0.5^{+0.4}_{-0.3}$

Notes.
[a] De Marco & Schmutz (1999); De Marco et al. (2000).
[b] Caraveo et al. (2001).
[c] Ducati (2002).
[d] Schröder et al. (2004).
[e] Apellániz et al. (2008).
[f] Pasinetti Fracassini et al. (2001).
[g] Gontcharov (2006).
[h] Van Leeuwen (2007).
[i] Soubiran et al. (2016).

(This table is available in machine-readable form.)

ORCID iDs

Alexandra C. Yep https://orcid.org/0000-0002-0909-6120
Russel J. White https://orcid.org/0000-0001-5313-7498

References

Apellániz, M. J., Alfaro, E. J., & Sota, A. 2008, arXiv:0804.2553v1
Bailer-Jones, C. A. L., Rybizki, J., Fouesneau, M., Mantelet, G., & Andrae, R. 2018, AJ, 156, 58
Baraffe, I., Chabrier, G., Allard, F., & Hauschildt, P. H. 1998, A&A, 337, 403
Baraffe, I., Homeier, D., Allard, F., & Chabrier, G. 2015, A&A, 577, 42
Basri, G., Martín, E. L., & Bertout, C. 1991, A&A, 252, 625
Bertoldi, F. 1989, ApJ, 346, 735
Bhatt, H. C. 1993, MNRAS, 262, 812
Biazzo, K., Alcalá, J. M., Frasca, A., et al. 2014, A&A, 572, 84
Brandt, J. C., Stetcher, T. P., Crawford, D. L., & Maran, S. P. 1971, ApJ, 163, 99
Briceño, C., Calvet, N., Hernández, J., et al. 2019, AJ, 157, 85
Bronfman, L., Nyman, L. A., & May, J. 1996, A&A, 115, 81
Cantat-Gaudin, T., Mapelli, M., Balaguer-Núñez, L., et al. 2019, A&A, 621, 115
Caraveo, P. A., De Luca, A., Mignani, R. P., & Bignami, G. F. 2001, ApJ, 561, 930
Castelli, F., & Kurucz, R. L. 2004, arXiv:0405087
Cazzoletti, P., Manara, C. F., Baobab Liu, H., et al. 2019, A&A, 626, 11
Chen, X., Bourke, T. L., Launhardt, R., & Henning, T. 2008, ApJ, 686, 107
Choi, J., Dotter, A., Conroy, C., et al. 2016, ApJ, 823, 102
Choudhury, R., & Bhatt, H. C. 2009, MNRAS, 393, 959
Cochran, W. D. 1988, ApJ, 334, 349
Cohen, M., & Kuhi, L. V. 1979, ApJS, 41, 743
Concha-Ramírez, F., Wilhelm, M. J. C., Portegies Zwart, S., & Haworth, T. J. 2019, MNRAS, 490, 5678
De Marco, O., & Schmutz, W. 1999, A&A, 345, 163
De Marco, O., Schmutz, W., Crowther, P. A., et al. 2000, A&A, 358, 187
De Vries, C. P., Brand, J., Israel, F. P., et al. 1984, A&AS, 56, 333
Delfosse, X., Forveille, T., Perrier, C., & Mayor, M. 1998, A&A, 331, 581
Dotter, A. 2016, ApJS, 222, 8
Dotter, A., Chaboyer, B., Jevremović, D., et al. 2008, ApJS, 178, 89
Ducati, J. R. 2002, yCat, 2237, 0
Eisner, J. A., Plambeck, R. L., Carpenter, J. M., et al. 2008, ApJ, 683, 304
Elmegreen, B. G. 2011, in EAS Publications Series 51, Star Formation in the Local Universe – EES2010, ed. C. Charbonnel & T. Montmerle (Les Ulis: EAS), 45
Fang, M., Kim, J. S., Boekel, R. Van., et al. 2013, ApJS, 207, 5
Fedele, D., van den Ancker, M. E., Henning, T., Jayawardhana, R., & Oliveira, J. M. 2010, A&A, 510, 72
Feiden, G. A. 2016, A&A, 593, 99
Gaia Collaboration, Brown, A. G. A., Vallenari, A., et al. 2018, A&A, 616, A1
Gaia Collaboration, Prusti, T., de Bruijne, J. H. J., et al. 2016, A&A, 595, A1
Gallet, F., & Bouvier, J. 2013, A&A, 556, 36
Gontcharov, G. A. 2006, AstL, 32, 759
Gray, D. 1992, The Observation and Analysis of Stellar Photospheres (Cambridge: Cambridge Univ. Press)
Gum, C. S. 1952, Observatory, 72, 151
Habing, H. J. 1968, BAN, 19, 421
Hartigan, P., Hartmann, L., Kenyon, S. J., Hewett, R., & Stauffer, J. 1989, ApJS, 70, 899
Hartigan, P., Kenyon, S. J., Hartmann, L., et al. 1991, ApJ, 382, 617
Hartmann, L., Herczeg, G., & Calvet, N. 2016, ARA&A, 54, 135
Herbig, G. H. 1974, PASP, 86, 604
Hernández, J., Hartmann, L., Megeath, T., et al. 2007, ApJ, 662, 1067
Hillenbrand, L. A. 2005, arXiv:astro-ph/0511083v1
Jeffries, R. D., Jackson, R. J., Cottaar, M., et al. 2014, A&A, 563, 94
Kajdič, P., Reipurth, B., Raga, A. C., & Walawender, J. 2010, RMxAA, 46, 67
Kim, J. S., Clarke, C. J., Fang, M., & Facchini, S. 2016, ApJ, 826, 15
Kim, J. S., Walter, F. M., & Wolk, S. J. 2005, ApJ, 129, 1564
Kuhn, M. A., Hillenbrand, L. A., Sills, A., Feigelson, E. D., & Getman, K. V. 2019, ApJ, 870, 32
Lindegren, L., Hernández, J., Bombrun, A., et al. 2018, A&A, 616, 2
Magazzú, A., Rebolo, R., & Pavlenko, Y. V. 1992, ApJ, 392, 159
Maheswar, G., & Bhatt, H. C. 2008, Ap&SS, 315, 215
Martín, E. L., Rebolo, R., Magazzú, A., & Pavlenko, Y. V. 1994, A&A, 282, 503
Meyer, M. R., Calvet, N., & Hillenbrand, L. A. 1997, AJ, 114, 288
Mohanty, S., Jayawardhana, R., & Basri, G. 2005, ApJ, 626, 498
Mortier, A., Oliveira, I., & van Dishoeck, E. F. 2011, MNRAS, 418, 1194
Nakatani, R., & Yoshida, N. 2019, ApJ, 883, 127
Neckel, T., & Staude, H. J. 1995, ApJ, 448, 832
Neuhäuser, R., Sterzik, M. F., Schmitt, J. H. M. M., Wichmann, R., & Krautter, J. 1995, A&A, 297, 391
Nidever, D. L., Marcy, G. W., Butler, R. P., Fischer, D. A., & Vogt, S. S. 2002, ApJ, 141, 503
O'Dell, C. R., Wen, Z., & Hu, X. 1993, ApJ, 410, 696
Palla, F., Randich, S., Flaccomio, E., & Pallavicini, R. 2005, ApJ, 626, 49
Palla, F., Randich, S., Pavlenko, Y. V., Flaccomio, E., & Pallavicini, R. 2007, ApJ, 659, 41
Paron, S., Ortega, M. E., Dubner, G., et al. 2015, AJ, 149, 193
Pasinetti Fracassini, L. E., Pastori, L., Covino, S., & Pozzi, A. 2001, A&A, 367, 521
Paxton, B., Bildsten, L., Dotter, A., et al. 2011, ApJS, 192, 3
Paxton, B., Cantiello, M., Arras, P., et al. 2013, ApJS, 208, 4
Paxton, B., Marchant, P., Schwab, J., et al. 2015, ApJS, 220, 15
Pecaut, M. J., & Mamajek, E. E. 2013, ApJ, 208, 9
Persi, P., Ferrari-Toniolo, M., Marenzi, A. R., et al. 1994, A&A, 282, 233
Pettersson, B. 1987, A&A, 171, 101
Pettersson, B. 2007, in Handbook of Star-forming Regions, Vol. 2, ed. B. Reipurth (San Francisco, CA: ASP)
Prato, L., Huerta, M., Johns-Krull, C. M., et al. 2008, ApJ, 687, 103
Rei, A. C. S., Petrov, P. P., & Gameiro, J. F. 2018, A&A, 610, A40
Reipurth, B. 1983, A&A, 117, 183
Reipurth, B., & Pettersson, B. 1993, A&A, 267, 439
Rieke, G. H., & Lebofsky, M. J. 1985, ApJ, 288, 618

Rodgers, A. W., Campbell, C. T., & Whiteoak, J. B. 1960, MNRAS, 121, 103
Sahu, M., & Sahu, K. C. 1992, A&A, 259, 265
Schröder, S. E., Kaper, L., Lamers, H. J. G. L. M., & Brown, A. G. A. 2004, A&A, 428, 149
Shu, F. H., Adams, F. C., & Lizano, S. 1987, ARA&A, 25, 23
Sicilia-Aguilar, A., Hartmann, L. W., Hernández, J., Briceño, C., & Calvet, N. 2005a, AJ, 130, 188
Sicilia-Aguilar, A., Hartmann, L. W., Szentgyorgyi, A. H., et al. 2005b, AJ, 129, 363
Sicilia-Aguilar, A., Kim, J. S., Sobolev, A., et al. 2013, A&A, 559, 3
Siess, L., Dufour, E., & Forestini, M. 2000, A&A, 358, 593
Skrutskie, M. F., Cutri, R. M., Stiening, R., et al. 2006, AJ, 131, 1163
Soubiran, C., Cantat-Gaudin, T., Romero-Gomez, M., et al. 2018, A&A, 619, A155
Soubiran, C., Le Campion, J.-F., Brouillet, N., & Chemin, L. 2016, A&A, 591, 118
Sridharan, T. K. 1992, ApA, 13, 217
Valenti, J. A., & Fischer, D. A. 2005, ApJ, 159, 141
Van Leeuwen, F. 2007, A&A, 474, 653
Vogt, S. S., Allen, S. L., Bigelow, B. C., et al. 1994, Proc. SPIE, 2198, 362
Walch, S., Whitworth, A. P., Bisbas, T. G., Wünsch, R., & Hubber, D. A. 2013, MNRAS, 435, 917
Walter, F. M., Brown, A., Mathieu, R. D., Myers, P. C., & Vrba, F. J. 1988, AJ, 96, 297
White, R. J., & Basri, G. 2003, ApJ, 582, 1109
White, R. J., & Ghez, A. M. 2001, ApJ, 556, 265
White, R. J., & Hillenbrand, L. A. 2004, ApJ, 616, 998
Winter, A. J., Clarke, C. J., Rosotti, G., et al. 2018, MNRAS, 478, 2700
Winter, A. J., Clarke, C. J., Rosotti, G., Hacar, A., & Alexander, R. 2019, MNRAS, 490, 5478
Zealey, W. J., Ninkov, Z., Rice, E., Hartley, M., & Tritton, S. B. 1983, ApL, 23, 119